NBSIR 80-1991

Materials for Fuel Cells

L. H. Bennett, C. K. Chiang, M. I. Cohen, A. L. Dragoo,
A. D. Franklin, A. J. McAlister

National Measurement Laboratory
National Bureau of Standards
U.S. Department of Commerce
Washington, D.C. 20234

Annual Report--January 1978 to December 1978

Issued March 1980

Prepared for
Division of Fossil Fuel Utilization
Department of Energy
Washington, D.C. 20545

NBSIR 80-1991

MATERIALS FOR FUEL CELLS

L. H. Bennett, C. K. Chiang, M. I. Cohen, A. L. Dragoo,
A. D. Franklin, A. J. McAlister

National Measurement Laboratory
National Bureau of Standards
U.S. Department of Commerce
Washington, D.C. 20234

Annual Report--January 1978 to December 1978

Issued March 1980

Prepared for
Division of Fossil Fuel Utilization
Department of Energy
Washington, D.C. 20545

U.S. DEPARTMENT OF COMMERCE, Philip M. Klutznick, *Secretary*

Luther H. Hodges, Jr., *Deputy Secretary*
Jordan J. Baruch, *Assistant Secretary for Productivity, Technology, and Innovation*

NATIONAL BUREAU OF STANDARDS, Ernest Ambler, *Director*

Tables

Table of Contents

Figures

ABSTRACT

Transition metal-metalloid compounds involving V, Mo, Ta, and Nb with P, Si and N were examined as potential electrocatalyts in hot concentrated phosphoric acid. MoP, WP, $MoSi_2$, Mo_2N/MoN, and W_2N/WN were found to be stable in the absence of applied potentials. The W_2N/WN was non-conducting. $MoSi_2$ and Mo_2N/MoN were both inactive as catalysts and unstable under cathodic potentials. MoP and WP corroded at about 0.2 volts RHE. Only WP showed even mild activity as a hydrogen oxidation catalyst.

The electrochemical properties of $Mo_xW_{1-x}C$ electrodes were studied in some detail, and found to be independent of x for values of x near 0.7. The electrochemical behavior is very similar to that of WC, with about the same activity and the same indifference to CO poisoning.

Experiments are outlined for studying a possible "spillover" effect from Pt to $Mo_{1-x}W_xC$ and transition metal borides as supports, and for using a Raman spectroscopic technique for characterizing the electrochemical interface of transition metal-metalloid compound electrodes.

The preparation and characterization of high-density (99.6 to 99.8% of theoretical) Y_2O_3-doped CeO_2 ceramics is described. The material exhibits very sharp, single-phase, x-ray diffraction peaks, indicating good compositional homogeneity. The influence of various preparation methods on the sintering characteristics of powders of these materials is described. Chemical analytical techniques are given.

The frequency dependence of the total impedance of discs of Y-doped CeO_2 ceramic was used to separate the intrinsic impedance (internal to the grains) from that arising from inhomogeneities in the specimen, presumably grain boundaries.

The electrical properties of the inhomogeneities were very different for materials prepared from powders produced by mixing the oxides from those found when the powders were prepared by coprecipitation. A higher resistance and a much higher capacitance were found in the latter case.

The temperature dependence of the inhomogeneity resistance in the Y_2O_3-doped CeO_2 is somewhat different from that of the intrinsic resistance, and since these resistances are in series, the larger resistance dominates in a dc measurement. At low temperatures it is the inhomogeneity resistance that controls the dc data, but at higher temperatures the intrinsic resistance becomes the more important. Hence, an Arrhenius plot of the dc conductivity exhibits a break, as often seen in the literature on these materials. Only the portion at temperatures above the break, on this view, represents the true properties of the substance itself.

In the course of 4-probe dc conductivity measurements on some Y_2O_3-doped CeO_2 materials a slow voltage transient was observed under constant-current conditions. This transient appears to involve a solid state diffusion process.

Modifications to our automated electrochemical measurement system are described that allow 1). an increase of the mass data storage available to the system, so that the results of a number of repetitive runs can be stored and later examined and compared; 2). an increase in the maximum sensitivity when data are being acquired at high speed, as in pulse mode operation; and 3). the use of a complete driver system in the software to coordinate all its aspects, and also the use of Fast Fourier Transform techniques during pulse mode operations. These modifications are described in detail.

1. Introduction

The National Bureau of Standards has undertaken a program of research on materials for fuel cells and batteries. This program includes studies of electrocatalysis in liquid-electrolyte cells and of solid electrolytes, in high-temperature cells and in batteries. The overall objectives of the program are:

1. to provide data allowing selection of optimum materials for critical aspects of fuel cell operations;
2. to improve the measurement capability and standards for assessment of performance (e.g., efficiency of electrode processes and lifetime of components) of materials in fuel cells and batteries.

This report will describe the results for the second year of the program.

The Materials for Fuel Cells Program at NBS during this year consisted of three major elements, which taken together reinforce each other in techniques and concepts; these elements embrace:

i. electrocatalysis, especially hydrogen oxidation, on non-noble metals and alloys;

ii. degradation mechanisms involving solid oxygen-transporting electrolytes; and

iii. Development of instruments.

2. Subtask Reports

2.1 Electrocatalysis in Phosphoric Acid

Introduction

In most fuel cell applications a major contribution to the overvoltage, and therefore to a reduction in useful voltage and to efficiency, comes from electrode polarization. For use in hot H_3PO_4 no satisfactory substitutes for Pt have been found, but Pt is not completely satisfactory. In catalyst loadings sufficiently large to ensure adequate efficiency and lifetime it makes a significant contribution to the cost. At the anode its sensitivity to CO poisoning forces the use of higher temperatures and catalytic shift conversion in the fuel processing train. At the cathode a mixed potential situation seems to exist and the open-circuit voltage lies below what should be possible. Thus a continued study of electrocatalysis and electrocatalysts in H_3PO_4 is worthwhile. In our program we have elected to study refractory metal-metalloid compounds (e.g. WC) as potential anode catalysts, and also in the role of Pt catalyst supports, capitalizing on a possible synergistic effect.

2.1.1 Materials Survey

In 1978, a number of transition metal-metalloid compounds were examined for stability in hot concentrated (82 °C, .85 by weight) H_3PO_4, and materials of apparent stability examined for H_2 oxidation activity in $1M H_3PO_4$ at 23 °C. Monophosphides of W, Mo, and Nb were prepared in powdered form by the method of Ripley [1][1]. Mixtures of the metal chlorides and calcium phosphide were heated at 1200 °C under Argon for two hours, then leached in dilute HCl to remove debris. Crystal structures were verified by X-ray diffraction. MoP has the crystal structure of WC, a superior acid-stable non-noble H_2 oxidation catalyst.

---

[1] Figures in brackets indicate the literature references given at the end of this report.

WP and NbP have structures closely related to that of WC, differing in the mode of stacking of a basic trigonal cell. The disilicides of W, Mo, Ta, and NB, and the mixed nitrides Mo_2N/MoN and W_2N/WN were obtained commercially in powder form. Of these materials, MoP, WP, $MoSi_2$, and both nitrides appeared stable in hot concentrated H_3PO_4. Porous electrodes of these materials were prepared in the manner described in the next section and examined by cyclic voltammetry for catalytic activity and voltage stability in H_3PO_4 at room temperature. $MoSi_2$ and Mo_2N/MoN were inactive and unstable. The W nitride proved non-conducting. Both MoP and WP reacted at 0.2V vs RHE; WP showed a shift in the current in the presence of H_2 that might indicate mild H_2 oxidation activity, as illustrated in Fig. 1.

2.1.2 Electrocatalytic Studies of $Mo_{1-x}W_xC$ Alloys

Our previous method of preparing porous electrodes on teflon-[2] coated Au discs has been altered, owing to occasional contamination of the electrodes by catalytically active precious metal contaminants in the Au supports [2]. In our current method, weighed amounts of the sample powder are wetted with a known amount of diluted Teflon-30. This mixture is either prepared directly upon, or an aqueous slurry of the mixture dripped upon, a teflon layer supported on Ta sheet, then air dried. After sandwiching between Al foils, the electrodes are hot pressed at 3,000 pounds, and 310 °C for several minutes. The Al is then dissolved in 20% NaOH and the electrode thoroughly rinsed in distilled H_2O and air dried. The electrode and its teflon support are then lifted

---

[2] Certain commercial equipment, instruments, or materials are identified in this report in order to specify adequately the experimental procedure. In no case does such identification imply recommendation or endorsement by the National Bureau of Standards, nor does it imply that the material or equipment identified is necessarily the best available for the purpose.

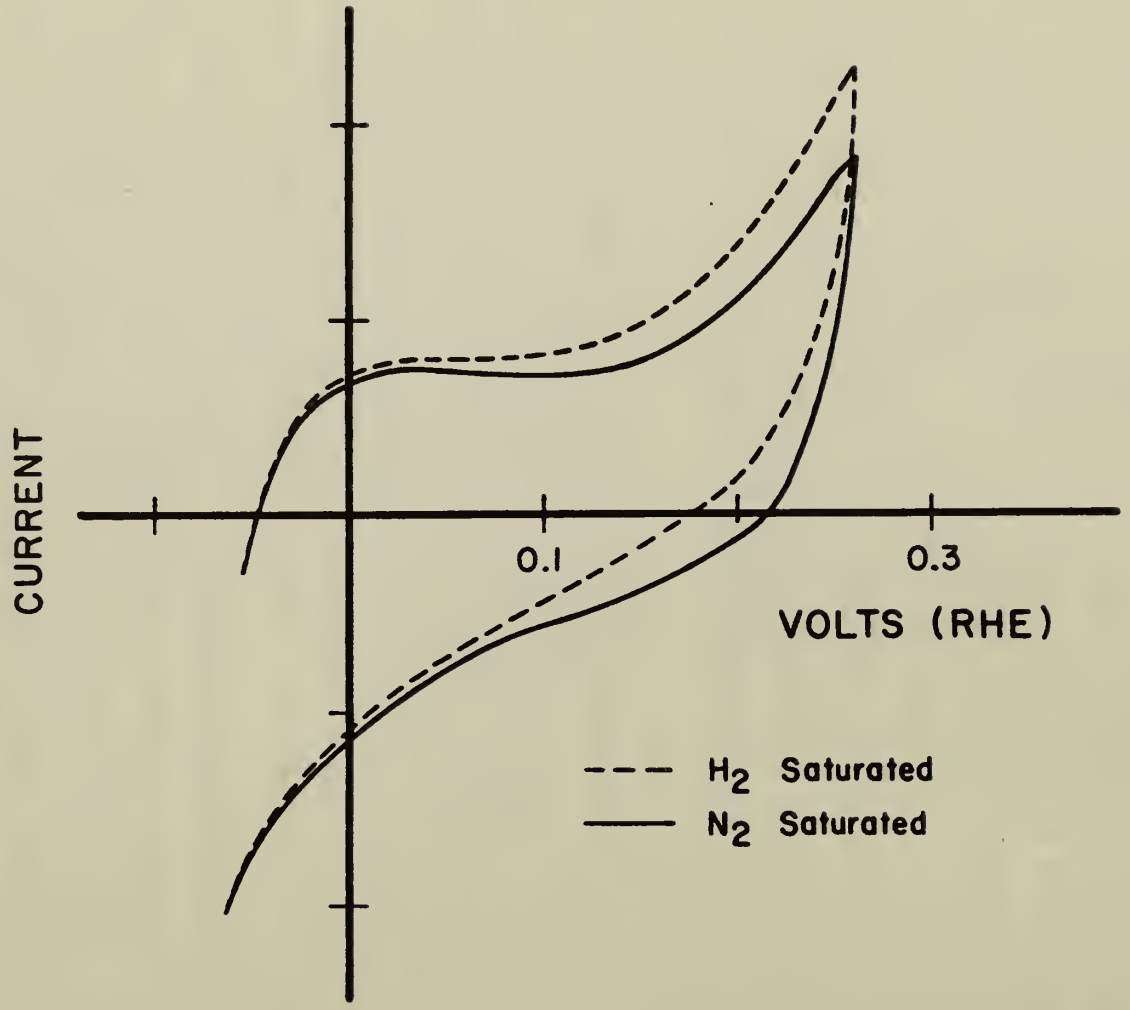

Figure 1. Voltammetric sweeps of a porous electrode of WP in N_2- and H_2-saturated 1M H_3PO_4 at 22 °C, showing evidence of H_2 oxidation activity. Sweep rate is 10.4 mV/sec.

from the Ta sheet. Under test, the bare electrode surface is exposed to gas-saturated electrolyte, with electrical contact made at the edges with a foil of Ta, which we have shown [3] to be passivated in the voltage range of interest here.

Four different production lots of $Mo_{0.7}W_{0.3}C$ and one of $Mo_{0.8}W_{0.3}C$ (kindly supplied by the manufactuer, Wa Chang-Teledyne Corp.) were examined for H_2 oxidation activity. As received, the refractory metal powders are contaminated to varying extents by Fe picked up in the finishing process, and by varying amounts of Ni and/or Co, used as catalysts in the forming reaction. These latter contaminants are insoluble in the compound lattice, and tend to wet the surface of the sample particles. Cleanup was accomplished by successive leachings in hot H_3PO_4 and washings in distilled H_2O, until no staining of the acid occurs. Porous electrodes were fabricated in the manner described above, with minimal teflon bonding, total teflon content being $\sim$4% by weight.

Current voltage characteristic curves of these $Mo_xW_{1-x}C$ electrodes were obtained in N_2- and H_2-saturated 1M H_3PO_4 at 22 °C. As all electrodes behaved similarly, only a sample curve for H_2 oxidation current vs. voltage for x = 0.7 is shown in Fig. 2. No difference in performance was observed for different values of x. Electrode performance is consistent with that expected for porous electrodes of catalysts obeying Butler-Volmer kinetics [4] up to about 0.3 V(RHE). The roll off above 0.3 V is not associated with diffusion-limited maximum current densities (judging from the far higher currents produced on Pt sheet under similar experimental conditions). Rather, it appears to be due to a drop in activity associated with reversible change in the chemical state of the catalyst surface at this potential. Linear voltammetric scans of an x =

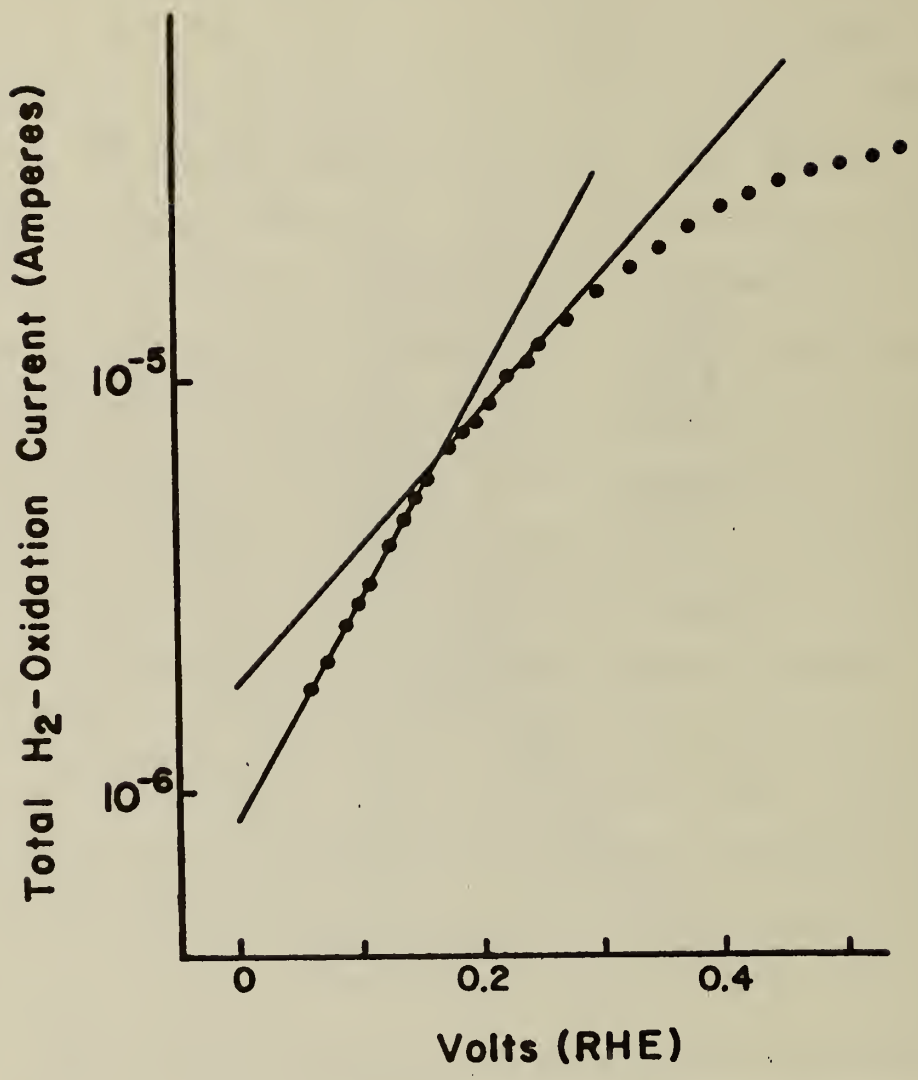

Figure 2. Hydrogen oxidation current vs. voltage for a thin porous electrode of $Mo_{0.7}W_{0.3}C$. The first straight line segment corresponds to a region of pure activation control; the second to mixed activation and diffusion control. The round off at higher voltage arises, not from diffusion limitations, but from a decrease in activity associated with chemical change of the catalyst surface.

0.7 sample at various sweep rates, shown in Fig. 3, lend support to this view. At lower sweep rates, the oxidation-reduction peak separation approaches Nicholson's limit [5] of 60 mV for unit charge exchange. Exchange current densities and Tafel slopes can be extracted from steady state current voltage characteristics, and are tabulated for $Mo_{1-x}W_xC$ samples at room temperature in 1M H_3PO_4 in Table 1.

Table 1

Electrochemical parameters for several $Mo_{1-x}W_xC$ electrodes, obtained in 1M H_3PO_4 at 22 °C.

Sample	b (volts)	b' (volts)	I_o (Amperes)	A (cm^2)	I_o/A (Amp/cm^2)
$Mo_{0.7}W_{0.3}C$-3	.19	.43	2.3×10^{-6}	23	1.0×10^{-7}
$Mo_{0.7}W_{0.3}C$-5	.19	.30	0.85×10^{-7}	11	$.8 \times 10^{-7}$
$Mo_{0.7}W_{0.3}C$-6	.18	.36	3.6×10^{-6}	36	1.0×10^{-7}
Mean of above	.19	.36			0.9×10^{-7}
$Mo_{0.8}W_{0.2}C$-1	.19	.40	1.8×10^{-6}	18	1.0×10^{-7}

Symbols:

b = Tafel slope

b' = slope of Tafel plot in region of mixed activation and diffusion control

I_o = Exchange current

A = Active area, inferred from manufacturer's stated mean particle size.

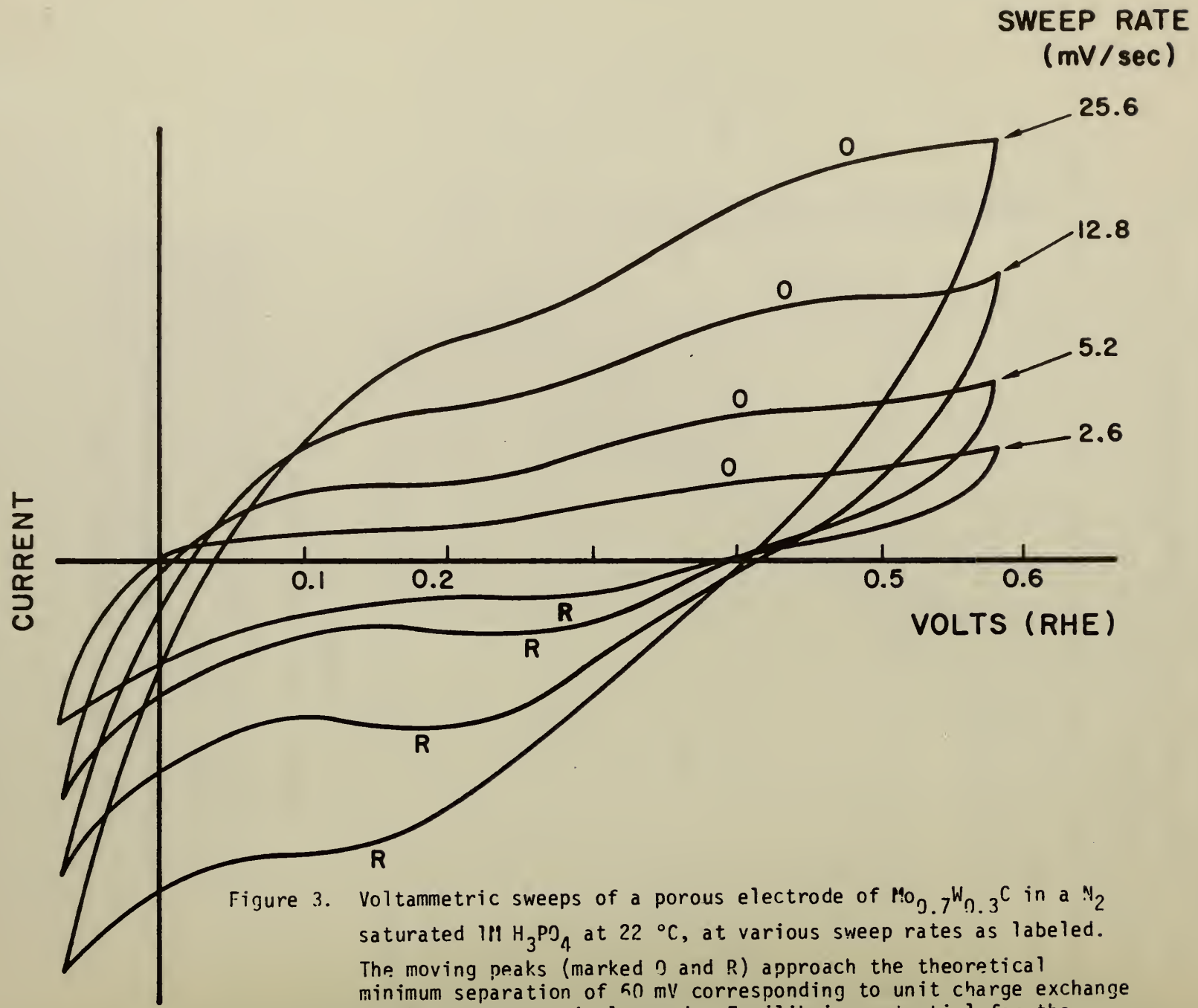

Figure 3. Voltammetric sweeps of a porous electrode of $Mo_{0.7}W_{0.3}C$ in a N_2 saturated 1M H_3PO_4 at 22 °C, at various sweep rates as labeled. The moving peaks (marked O and R) approach the theoretical minimum separation of 60 mV corresponding to unit charge exchange as the sweep rate is lowered. Equilibrium potential for the surface reaction is 0.32 ± 0.03 (RHE).

Further valuable information can be obtained from current-voltage characteristics obtained at various temperatures. One of the x = 0.7 electrodes, and an electrode of WC (prepared by reacting WO_3 with lampblack at 1200 °C for two hours in flowing H_2) were studied in 85% H_3PO_4 at 50, 70, 90, and 115 °C. Rate parameters and apparent activation energies extracted from these measurements are tabulated for $Mo_{0.7}W_{0.3}C$ in Table 2 and for WC in Table 3. In addition, measurements were performed on the x = 0.7 sample with a fuel feed containing 3% CO at the same four temperatures. The CO had no detectable effect on the H_2 oxidation current. (Pt sheet, however, was completely poisoned under these conditions.)

Table 2

H_2-oxidation rate constants and apparent acitvation energies for $Mo_{0.7}W_{0.3}C$ in 85% H_3PO_4.

°C	$10^3/T$ (K^{-1})	b (volts)	b' (volts)	$\frac{10^3 b}{T}$	b'/b	I_o (Amp)	i_o (A/cm^2)
50	3.096	.245	.462	0.768	1.886	$.16\times10^{-5}$	0.4×10^{-7}
70	2.907	.282	.633	0.820	2.245	$.71\times10^{-5}$	2.0×10^{-7}
89	2.766	.257	.490	0.716	1.892	1.10×10^{-5}	2.8×10^{-7}
115	2.577	.340	.645	0.876	1.898	3.10×10^{-5}	8.6×10^{-7}
				mean: 0.795	mean: 1.980		

E_a = 8.3×10^3 cal/mol. from current at 0.2 volts (RHE)

10.5×10^3 cal/mol. from I_o

Table 3

H_2-oxidation rate constants and apparent activation energies for for WC in 85% H_3PO_4

°C	$10^3/T$ (K^{-1})	b $(volts)^{-1}$	b' $(volts)^{-1}$	$\frac{10^3 b}{T}$	b'/b	I_o (A)	i_o (A/cm^2)
50	3.096	.201	.321	0.622	1.597	0.09×10^{-5}	0.3×10^{-7}
70	2.907	.302	.579	0.878	1.917	0.44×10^{-5}	1.7×10^{-7}
89	2.766	.244	.521	0.675	2.135	0.47×10^{-5}	1.8×10^{-7}
115	2.577	.353	.794	0.910	2.249	1.70×10^{-5}	6.6×10^{-7}
				mean: 0.771	mean: 1.974		

E_a = 6.8×10^3 cal/mol from current at 0.2 volts (RHE)

10.7×10^3 cal/mol from I_o

2.1.3 Refractory Hard Metals as Pt Catalyst Supports

The catalytic activity of Pt has been found to be promoted on certain supports (on perovskites for CO oxidation [6] and on sodium tungsten bronze for O_2 reduction [7]). It is of considerable interest and some practical significance to inquire whether any benefits might accrue from supporting Pt on $Mo_{1-x}W_xC$ alloys. It is known that the Group VIII metals Co and Ni wet WC, though they are insoluble in it. If Pt behaves similarly, it may disperse stably, on an atomic scale, over the WC surface, perhaps forming a well defined Pt-WC surface alloy. In addition to such geometric promotion, there is the possibility that, since WC is insensitive to CO poisoning, spillover of adsorbed CO onto the WC support may occur, even if the supported Pt is clustered, with subsequent improvement of the catalytic efficiency of Pt in the presence of CO. Several methods can be employed in the fabrication of $Mo_{1-x}W_xC$

supported Pt catalysts:

a). precipitation and reduction of a Pt salt on the compounds;

b). alloying of Pt with the base metal(s) before carburization (∿1% of Pt is soluble in W at 200 °C, e.g.);

c). doping of an oxide precursor before caburization;

d). electrochemical deposition of Pt upon $Mo_{1-x}W_xC$.

Apparatus is being completed to carry out these preparative methods.

We have observed [3] that several metallic transition metal borides remain passivated at remarkably high potentials at room temperature. It is of considerable interest to investigate the stability of these materials as Pt supports at high potential and temperature in the presence of O_2 in concentrated H_3PO_4. Some contribution to the problem of carbon support corrosion on the air side of phosphoric acid cells may be made in this way. The preparative techniques outlined above should prove useful here.

We are testing the Raman technique as a method for characterizing the electrochemical interface of transition metal-metalloid compound electrodes. We have carried out a preliminary study of the Raman spectrum of WC in air, and observed the presence of small amounts of W in the +6 oxidation state. Further encouragement comes from the work of other investigators who have observed Raman spectra in air of related compounds (TiN, TiC, ZrN, NbC, NbN, and V_3Si [8]) via defect-induced scattering of radiation whose wavelength falls in a region of low reflectivity, hence of higher than average sample penetration. This strongly suggests that surface alloying on WC should be observable via impurity vibrational bands. We are preparing a half cell suitable for these Raman investigations.

2.2 High Temperature Solid Electrolytes

Introduction

Oxide solid solutions having a defective fluorite structure and based on ZrO_2, CeO_2, and ThO_2, doped with CaO, Y_2O_3 or the trivalent rare earth oxides, have high oxygen ion mobilities relative to the pure constituent oxides. The high oxygen ion mobilities make these oxide solid solutions potentially useful solid electrolytes for high temperature fuel cells. The high oxygen ion mobility results from the large concentration of oxygen vacancies introduced into the oxygen sublattice of the host oxide, about 5 to 15 mole % of dopant may be added depending upon the oxide system.

ZrO_2-based solid solutions have been used as electrolytes for high-temperature electromotive force measurements since the mid-1930's [9,10], and ThO_2-based electrolytes, since 1957 [11]. ZrO_2-based electrolytes have been studied for fuel cell applications principally at Westinghouse and G. E. in the United States, and elsewhere in France, Germany and the Soviet Union. Recent results [12, 13] on CeO_2:Ln_2O_3, where Ln represents a variety of lanthanide ion or Y^{3+}, have revealed oxygen-ion conductivities essentially equivalent to that of ZrO_2:CaO but at temperatures about 200 °C lower. Thus, fuel cells using a CeO_2-based electrolyte might operate at about 800 °C as compared to 1000 °C for ZrO_2-based electrolytes. However, Ce-based electrolytes begin to show appreciable electronic conduction at higher oxygen partial pressures than do the ZrO_2-electrolytes; for example, one-half of the electrical conductivity is electronic in $(CeO_2)_{0.95}(Y_2O_3)_{0.05}$ at $P_{O_2} = 10^{-14}$ atm ($\sim 10^{-19}$ Pa) for T = 800 °C, whereas for ZrO_2:CaO, $P_{O_2} = 2.5 \times 10^{-31}$ atm (2.5×10^{-36} Pa) for T 1000 °C [14].

At the high oxygen vacancy concentrations present in these electrolytes, the oxygen vacancies are probably nearly all associated with the dopant cations [15]. If these electrolytes undergo prolonged anneals at moderate

temperatures (<1000 °C), the oxygen vacancies, and perhaps to a lesser extent, the dopant cations, may order into a structure coherent with the fluorite structure of the host oxide. Formally, in terms of a coherent structure, the ionic conductivity of the electrolyte may decrease (resistance may increase) because the vacancies, relative to the fluorite structure, must then move cooperatively.

The existence of coherent structures is well documented for ZrO_2-based solid solutions [16-23]. Coherent structures in CeO_2-based solid solutions have not been identified.

Carter and Roth [20] found that the increase in resistance of calcia stabilized (CSZ) when annealed at <1000 °C was associated with the formation of coherent structures, observed as superstructure in neutron and x-ray diffraction. This "aging" of CSZ could be reversed ("deaged") by annealing at 1400 °C. In a high temperature fuel cell aging of the electrolyte would reduce the efficiency of the cell.

A second aging process which may alter the long-term performance of a high temperature fuel cell electrolyte is the redistribution of the dopant cations along the grain boundaries. Relative to the lattice, the dopant cations appear as negative charges. Thus, they can be expected to migrate under the influence of an applied field. Although the mobility of these cations within the interior of the grain is negligibly small for practical purposes, their mobility in the grain boundaries can be significant. For example, from the tracer diffusion measurements for Ca^{2+} ions in CSZ [24], the time required for Ca^{2+} ions to cross a 20 μm thick electrolyte film with a potential difference of 0.8 V is on the order of hundreds of years. On the other hand, the same tracer diffusion

study showed that migration of Ca^{2+} ions in the grain boundaries is perhaps 1000 times larger at 1800 °C than the bulk diffusion rate, a ratio that would be expected to be even larger at lower temperatures. Hence, migration of the dopant ions along grain boundary paths over significant distances during times of the order of a year or less can be expected in all of the fluorite-structure oxides of current interest as solid electrolytes.

The migration of dopant ions along grain boundaries can be expected to result in at least three deleterious effects: (1) a build-up of a resistive layer at either electrolyte boundary, (2) a build-up of a space charge at the electrodes resulting effectively in an overvoltage, and (3) a possible interference with the electrode reaction due to a change in electrolyte composition at the electrolyte-electrode boundaries.

The NBS program of studies on high-temperature electrolytes currently contains two elements: a study of degradation mechanisms in CeO_2-based oxygen-ion electrolytes, and the development of the impedance measurement as a method of analyzing fuel cell performance with the particular aim of developing a lifetime-prediction test.

2.2.1 Electrolyte Materials

Preparation and Characterization of High-Density Ceria-Yttria

Using the carbonate process described in the previous report (NBSIR-78-1472) about 880 g of ceria-yttria powder was prepared by coprecipitation of the carbonates from homogeneous solution; the carbonate process is illustrated schematically in figure 4. The oxide powder which was obtained by calcining the carbonate to 600 °C had the nominal composition $Ce_{0.90}Y_{0.10}O_{1.95}$. About 450 g of this powder was formed into a billet; the billet was isostatically pressed at 69 MPa (10,000 psi) and then was hot-pressed at 1350 °C and 28 MPa (4000 psi) for 3/4 hour. The resulting ceramic was beige color, had a glassy luster and fractured conchoidally. The bulk density was 99.6 to 99.8 percent of theoretical (densities will be expressed as a percentage of theoretical, the lattice density calculated from the x-ray lattice parameters and the mass of the contents of the unit cell for the appropriate composition). The billet has cracked into several pieces during the hot-pressing, apparently as a result of excessive shrinkage and adherence of part of the billet to the walls of the die.

Figure 5 shows a SEM micrograph of an etched fracture surface of the hot-pressed material. The grains are equiaxed; only a small amount of porosity is evident; and the fracture has occurred along the grain boundaries.

Specimens were cut from the billet and were polished, cleaned, etched and examined by optical microscopy and x-ray diffraction. Thick specimens were observed to be translucent to the beam of the microscope; thin sections, about 50 μm thick, were transparent. This optical quality is consistent with the nearly theoretical density of the specimens. The x-ray diffraction patterns showed very sharp fluorite structure peaks, the K_{α_1}-K_{α_2} doublet was clearly resolved for $2\theta > 50°$, indicating good homogeneity. Estimates of the lattice parameter suggested that the yttrium content was less than 10 atom-percent of the cation content.

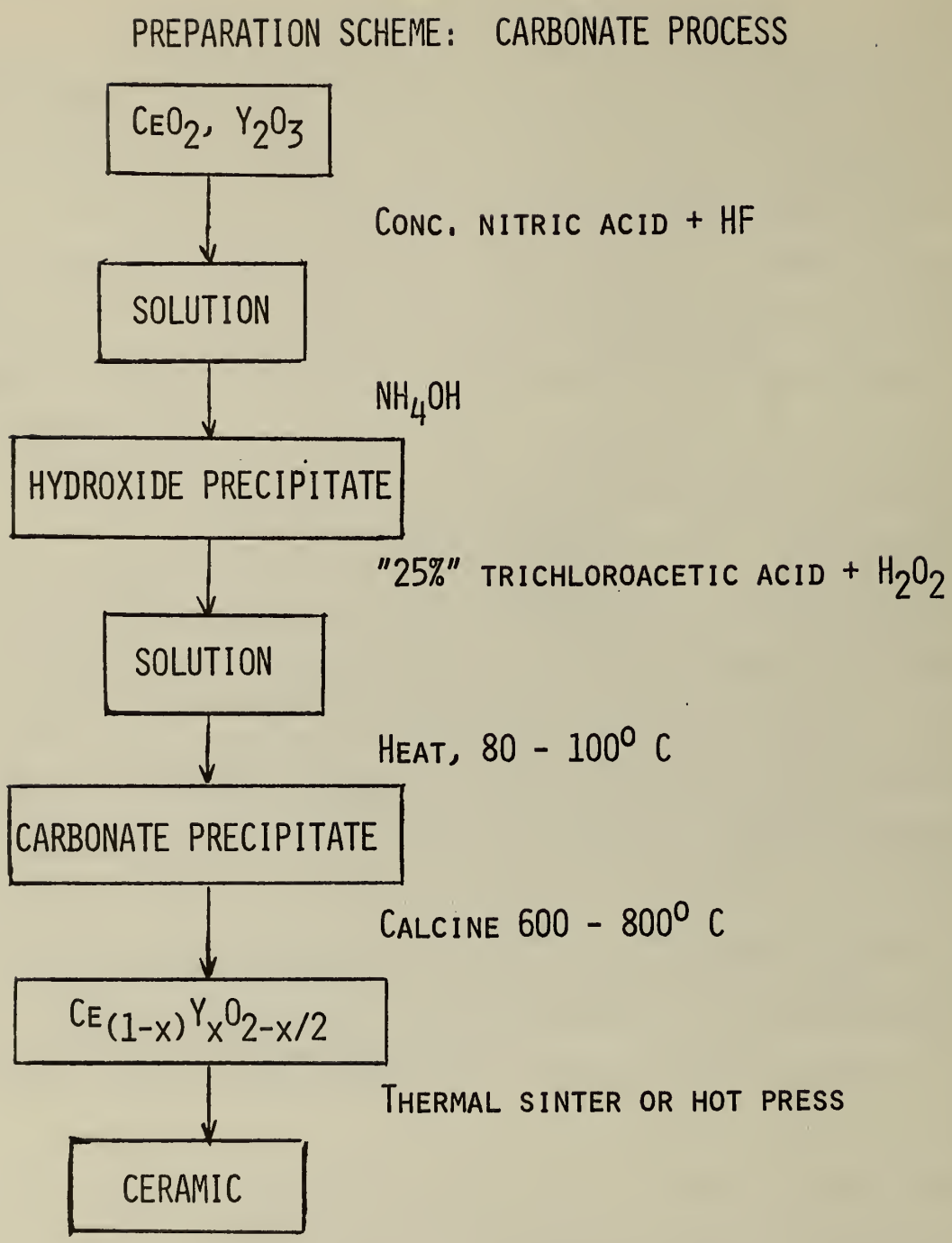

Figure 4. Preparation Scheme: Carbonate Process.

Figure 5. Fracture Surface of hot-pressed ceria-yttria ceramic.

The shrinkage during hot-pressing may be affected (1) by the reactivity of the powder, which may be adjusted by chemical preparation and by calcining the powder prior to hot-pressing; (2) by the extent to which the powder is compacted in forming the green body; and (3) by the temperature and pressure during the hot-pressing stage. To study the shrinkage, or densification, a sintering study was carried out. Powders were prepared by the carbonate process, by a tartaric acid-ethylene glycol (TA-EG) resin process and by a citric acid (CA) resin process. Powder samples from the carbonate process were calcined at 600, 700, 800, 900 and 1000 °C for about six hours; powder samples from the other two processes were calcined at 800 °C for about six hours. Isostatic pressing to 69 MPa (10,000 psi) was used to compact further some of the specimens. Specimens were randomly selected for the sintering anneals. Anneals #1 to 3 were carried out at about 1510 °C for 24 hours. During the fourth anneal the furnace burned out at about 1500 °C. Anneals #5 and 6 were carried out in a second furnace at about 1550 °C for 24 hours. Bulk densities were measured by an Archimedes technique with mercury as the buoyant medium; each sample was measured three times to obtain an estimate of the measurement error.

Relative treatment effects with associated 80 percent confidence intervals were calculated from the data.

For the chemical processing effects, the TA-EG resin process did not differ significantly from the carbonate process; whereas, the CA resin process yielded a powder slightly less sinterable than the powder from the carbonate process, resulting in a loss of density amounting to 4 ± 2 percent of theoretical.

The effects due to calcination temperature were compared to the treatment effect at 600 °C. Calcining at 700 °C resulted in a loss of density in the final ceramic of about 12 ± 8 percent of theoretical, whereas, calcining at 800 °C may have improved the powder slightly, the increase in density being 4.4 ± 4.2 percent of theoretical. Calcining at 900 and 1000 °C did not significantly alter the densification as compared to the 600 °C treatment.

Isostatic compaction of the green bodies improved the final relative densities by 15 ± 5 percent of theoretical. Green densities before isostatic pressing were 40 to 50 percent of theoretical; after pressing they were 60 to 70 percent of theoretical.

Final densities were significantly higher, 13 ± 5 percent of theoretical, for specimens sintered at 1550 °C in the second furnace as compared to those sintered at about 1510 °C in the original furnace. As expected, the densities of specimens from the aborted anneal, #4, were the lowest, the relative treatment effect being -14 ± 9 percent of theoretical.

The best densities are summarized in table 4.

Table 4

Summary of Best Densities of Y_2O_3-doped CeO_2 Ceramics

Powder Preparation	Sintering Process	Density, % of Theoretical
Carbonate Process	Thermal	95.4 ± 3.4*
Carbonate Process	Hot-Press	99.5
TA-EG Resin Process	Thermal	95.2 ± 2.8
CA Resin Process	Thermal	89.0 ± 2.6

*Standard deviation.

Development of Analytical Methods

The possible loss of some yttria in the preparation of the oxide powder by the carbonate process indicated the need for routine analytical procedures to verify the compositions of solutions and powders.

To analyze solutions for Ce and Y, an analytical procedure and standard solutions were developed for atomic emission spectroscopy. Cerium concentrations can be measured in the range of 100 to 500 μg/ml; yttrium, in the range of 1 to 25 μg/ml.

For the analysis of the oxide powders work was begun on the development of a procedure and of standards for x-ray fluorescence analysis. Lytle and Heady [25] described an x-ray fluorescence analysis of high-purity rare earth oxides. They prepared their standards by coprecipitation of mixtures of rare earths as oxalates and then converting the oxalates to oxides. In preparing the oxalates we have chosen to use a method developed by Carron, Skinner and Steven [26] who homogeneously coprecipitated rare earths from solution using the hydrolysis of dimethyl oxalate to generate the oxalate ion. They prepared the dimethyl oxalate reagent by refluxing dehydrated oxalic acid in methanol.

This coprecipitation technique yielded a precipitate that settled rapidly. When the precipitate was dried, a fine white powder was obtained. Figure 6 is a micrograph of a particle of the oxalate powder. X-ray diffraction analysis of this powder showed many low angle peaks, some of which could be assigned to the monoclinic structure of $Ce_2(C_2O_4)_3 \cdot 10H_2O$ but with small changes of the lattice parameters, suggesting some incorporation of yttrium into the structure. However, a second phase was found to be present as indicated by the strongest diffraction peaks which could not be indexed with the monoclinic pattern.

Figure 6. Cerium-yttria oxalate obtained by coprecipitation from a homogeneous solution.

Upon calcining to 650 °C a fine yellow powder was obtained. Figure 7 shows a micrograph of this powder. The powder retained the shape and twinning features of the oxalate precursor. However, x-ray diffraction analysis clearly showed that the powder had been transformed to the fluorite structure.

Acknowledgements

We wished to thank Ms. Bethanne Warrack for her assistance with this work and, in particular, for her development of analytical procedures and standard solutions for atomic emission analysis of solutions.

Figure 7. Cerium-yttrium oxide obtained by calcining the oxalate to 650 °C.

2.2.2. Impedance Measurements

Introduction

We are studying the use of impedance measurements, using a network analyzer operating in the frequency range from 10 Hz to 13 MHz, as a method of characterizing solid electrolyte cells. To date, we have concentrated on the bulk properties of the electrolyte, using sputtered Pt electrodes and working in an atmosphere containing either air or oxygen-argon mixtures ranging in oxygen partial pressure from 1 to about 10^{-4} atm, at temperatures from about 200 °C to about 800 °C. These measurements appear to be interpretable in terms of a simple equivalent circuit, shown in Fig. 8. In this circuit, Cg is the geometric capacitance of the specimen, R_B the resistance arising from the intrinsic transport process of the crystalline grains, and Z^*_{gb} the impedance arising from inhomogeneities such as grain boundaries. We find the latter can be represented using a Cole-Cole [27] equation:

$$Z^*_{gb} = \frac{\Delta Z_{gb}}{1+(j\omega\tau)^{1-\alpha}} \qquad (1)$$

where ΔZ_{gb} is the contribution of the inhomogeneities to the dc resistance, τ the most probable time constant, and α is a measure of the width of the distribution of time constants. The circular frequency is ω. The electrode impedance is indicated by Z^*_{el}. Little work has been done on Z^*_{el} during the past year and it will not be discussed further here. We expect a post-doctoral fellow (James Bethin, from the University of Illinois) to join the group early next year to begin studies of electrode effects.

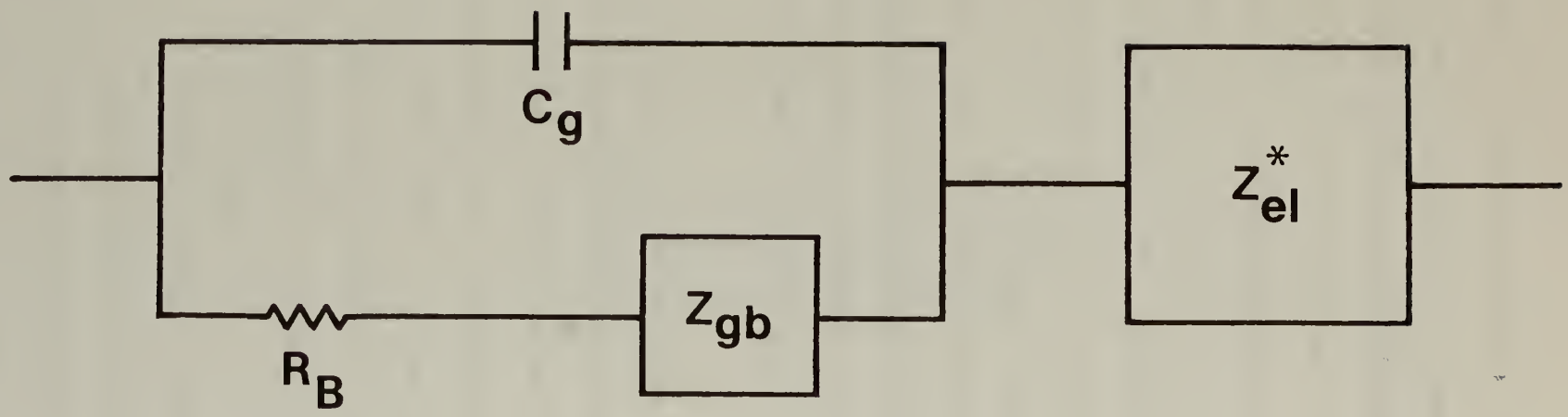

Figure 8. Equivalent circuit for Y_2O_3 doped CeO_2 ceramic specimens with Pt electrodes.

In principle, in CeO_2 heavily doped with Y_2O_3 only ionic conduction is expected within the range of precision of these measurements. Tuller and Nowick [12] show negligible deviation from unity of the ionic transport number for 10% of the Ce^{4+} ions replaced by Y^{3+} for temperatures up to 1000 °C and atmospheres containing more than 10^{-5} atm oxygen. Thus, we expect that measured values for both R_B and ΔZ_{gb} should be independent of P_{O_2}, the oxygen partial pressure. This was found to be true for several sets of measurements at 250 °C for two specimens (5 sets for one, 7 for the other) as the oxygen partial pressure P_{O_2} was cycled between $\sim 10^{-.7}$ and $\sim 10^{-3.7}$ atm. (Quarterly Progress Report for 1 April 1978 to 30 June 1978).

Correlation of Preparation and Properties

Y_2O_3-doped CeO_2 ceramic specimens have been prepared under a variety of conditions, and we find that they fall clearly into two distinct types:

1. Specimens prepared by mixing the oxides CeO_2 and Y_2O_3 in powdered form, ball milling an alcohol slurry of the mixed oxides, calcining, and either isostatically pressing specimens at room temperature and sintering at temperatures up to 1550 °C for about 16 hours, or hot pressing at temperatures near 1350 °C for 3/4 hour. (Type M)
2. Specimens prepared by coprecipitating the combined oxides from solution, calcining, and either sintering or hot pressing as above. (Type C)

The impedance behavior for these two types, as revealed by plots of the impedance Z in the complex plane, are very different (Details are given in the Quarterly Progress Report for 1 July, 1978 to 30 September, 1978 where what is here labelled type M was called Type B. M and C stand for mixed and coprecipitated). In brief, and in terms of the parameters of eqn. 1,

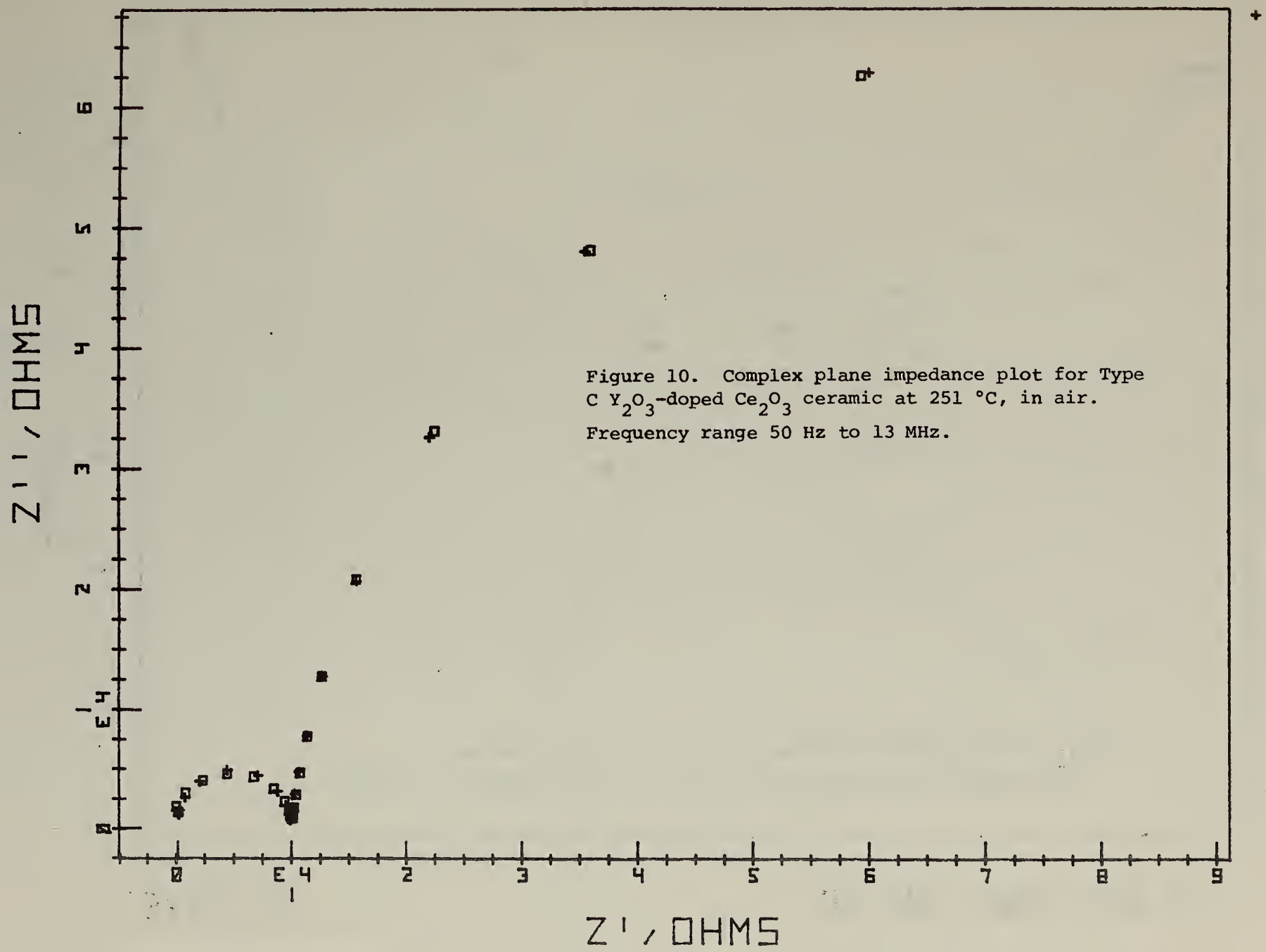

Figure 10. Complex plane impedance plot for Type C Y_2O_3-doped Ce_2O_3 ceramic at 251 °C, in air. Frequency range 50 Hz to 13 MHz.

Figure 9. Complex plane impedance plot for Type M Y_2O_3-doped Ce_2O_3 ceramic at 281 °C, in air. Frequency range 50 Hz to 13 MHz.

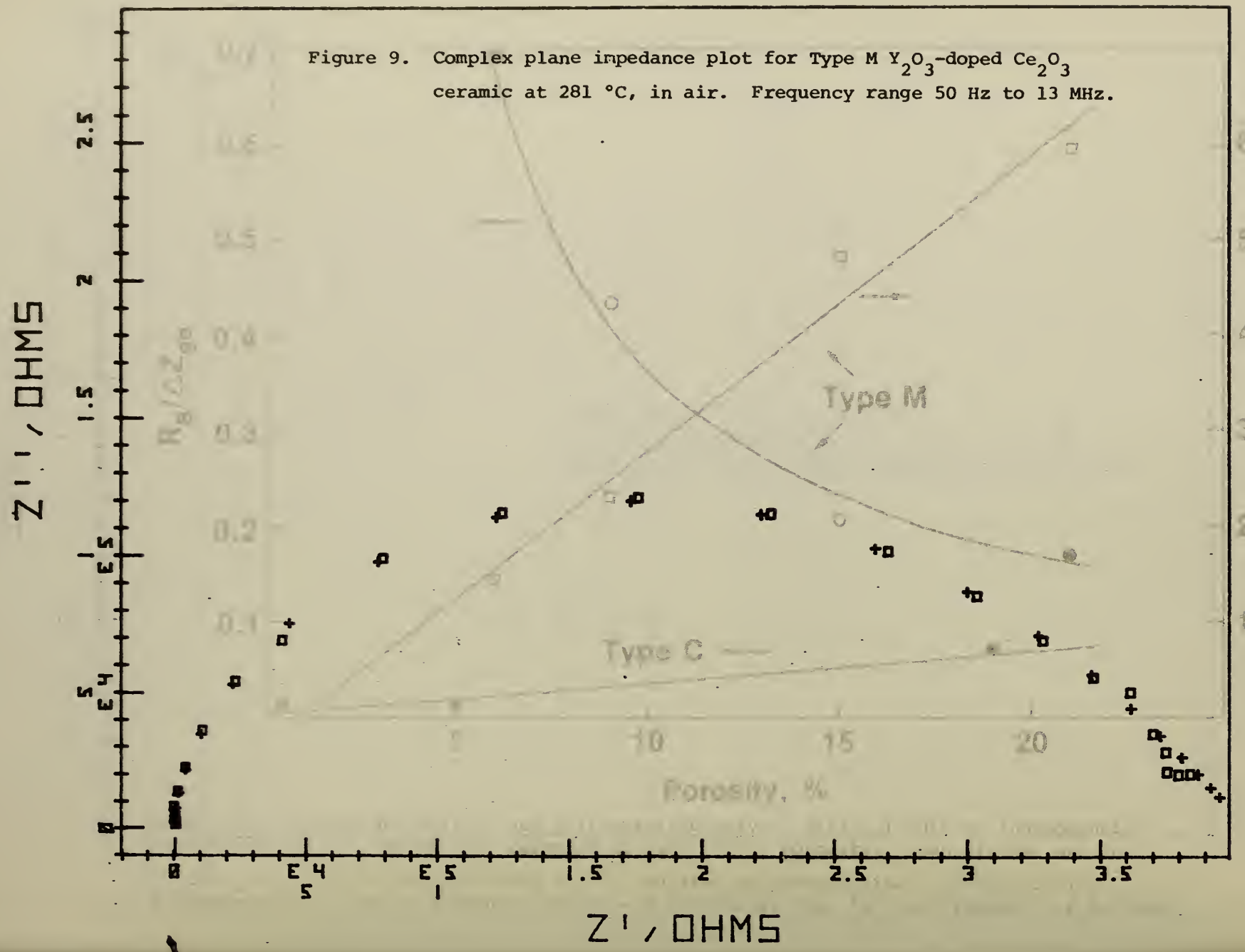

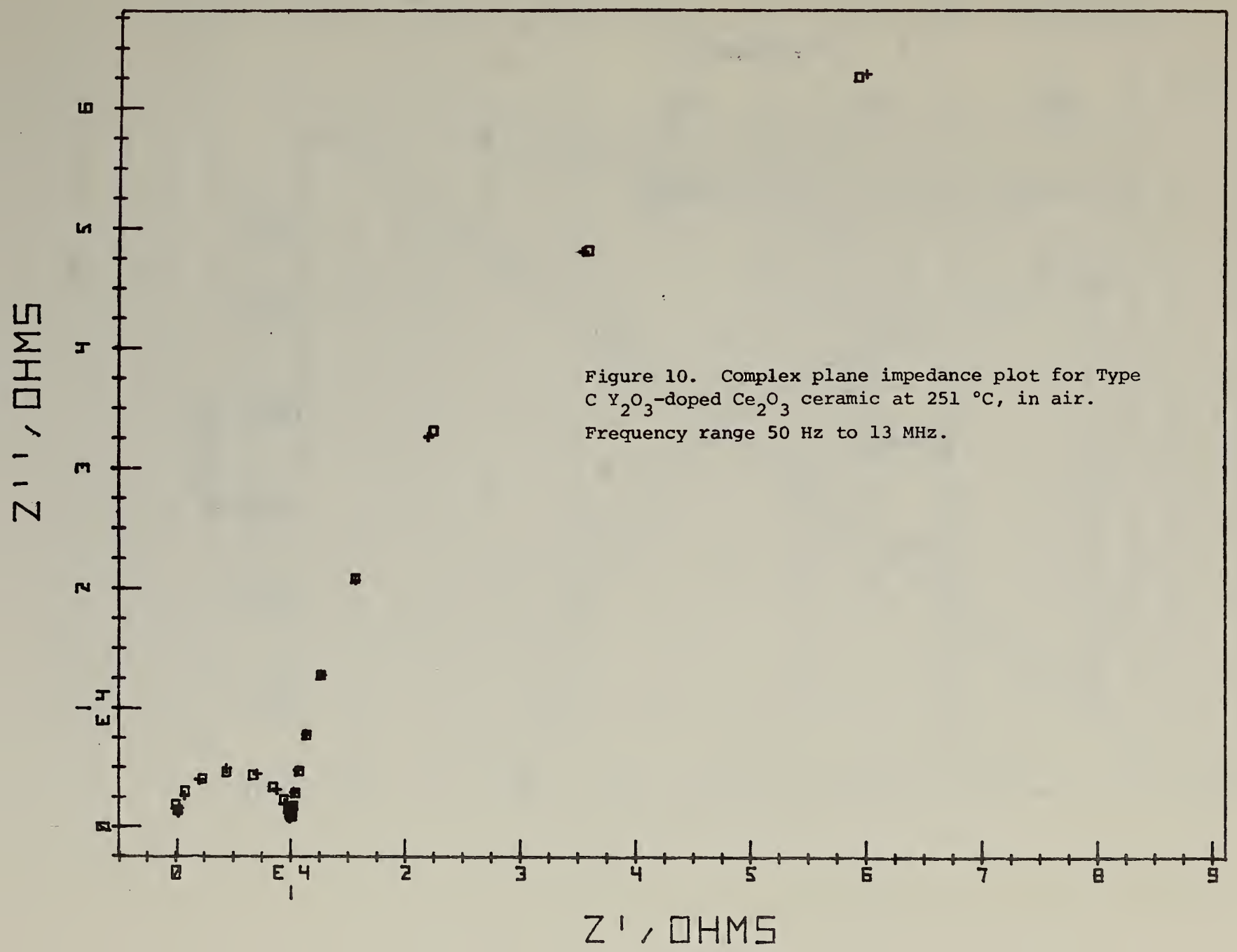

Figure 10. Complex plane impedance plot for Type C Y_2O_3-doped Ce_2O_3 ceramic at 251 °C, in air. Frequency range 50 Hz to 13 MHz.

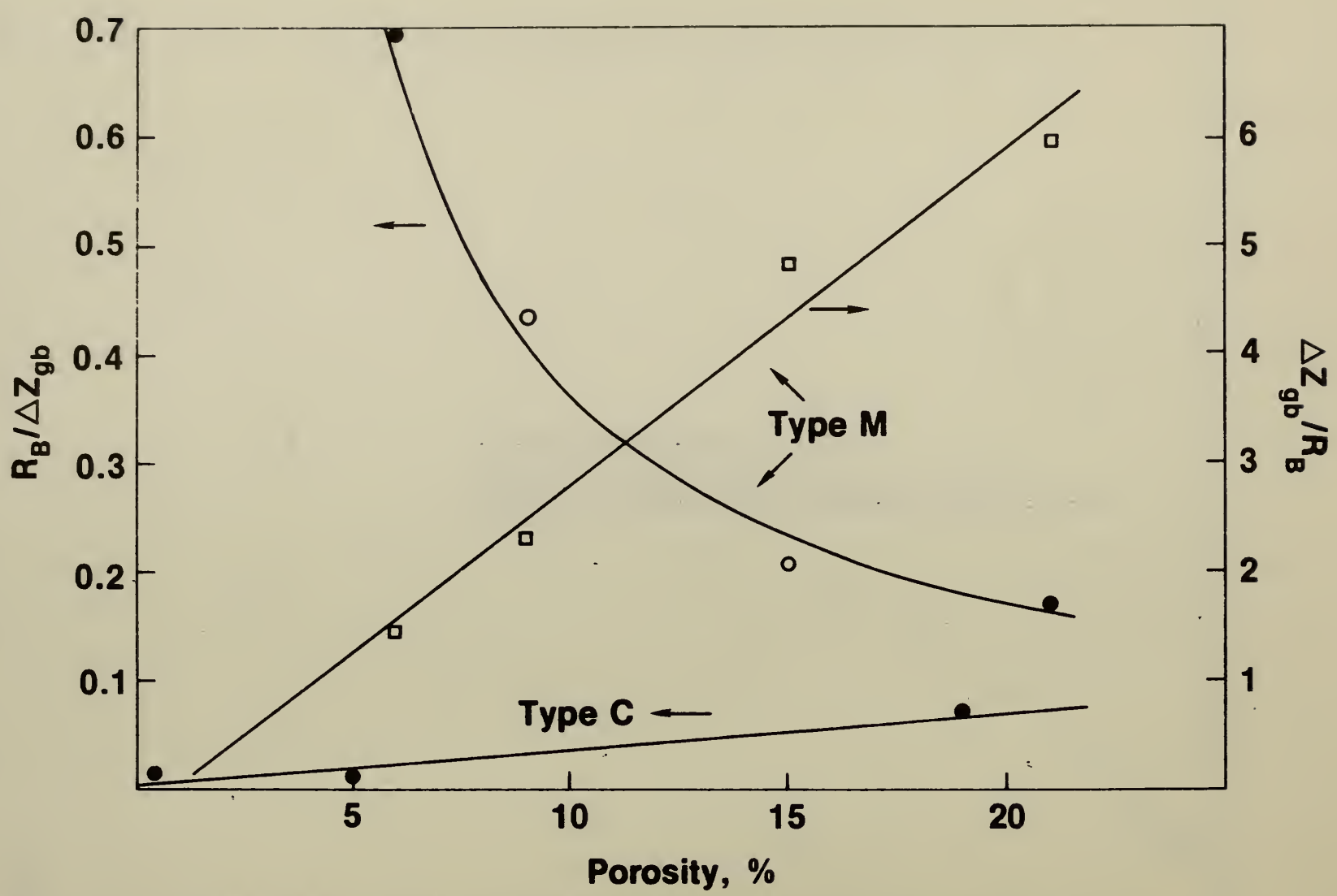

Figure 11. Circles and solid lines (illustrative only): Ratio of bulk to inhomogeneity resistances for Y_2O_3-doped CeO_2 ceramics at ~250 °C vs. porosity. Open circles are for 20 cation % Y^{3+}, rest for 10 cation % Y^{3+}. Squares and dotted line: Inverse ratio (inhomogeneity to bulk resistance) for Type M specimens, line is least squares fit to data.

$$\Delta Z_{gb}/R_B = -.36 + 31.3\ P, \tag{2}$$

where P is the volume fraction of pores. While the form of this equation is very similar to that expected for non-interacting spherical pores in an otherwise homogeneous conducting medium, the coefficient of P is very different. Juretschke et al. [28] have given for the effective conductivity σ_m of this model

$$\sigma_m = 2(1-P)\ \sigma_o/(2 + P) \tag{3}$$

where σ_o is the conductivity of the medium. This gives for $R_B + \Delta Z_{gb}$, the total low frequency resistance

$$R_B + \Delta Z_{gb} = \frac{G\sigma_o}{\sigma_m} = \frac{G(2+P)}{2(1-P)}, \tag{4}$$

where $G\sigma_o$ is the geometric factor. At high frequencies no internal fields due to the pores occur and

$$R_B = \frac{G}{1-P} \tag{5}$$

From eqns 4 and 5 we find

$$\Delta Z_{gb}/R_B = P/2. \tag{6}$$

Whereas this model would give a slope for the line in fig. 11 of 1/2, the experimental value is 31.3. Since pores are inclusions of the highest possible resistivity, this result suggests that no model based on a homogeneous conducting medium containing non-interacting inclusions of different conductivity can account for these data. Rather, the higher-resistivity material must consist of at least strongly interacting regions, even perhaps continuously connected.

Temperature Dependence of Resistances

We have examined in somewhat greater detail the values for R_B and ΔZ_{gb} for the two most porous specimens of each type. Figures 12 and 13 exhibit the temperature dependence of each quantity for the type M specimen (specimen B-3) and the type C specimen (B-7), respectively, in

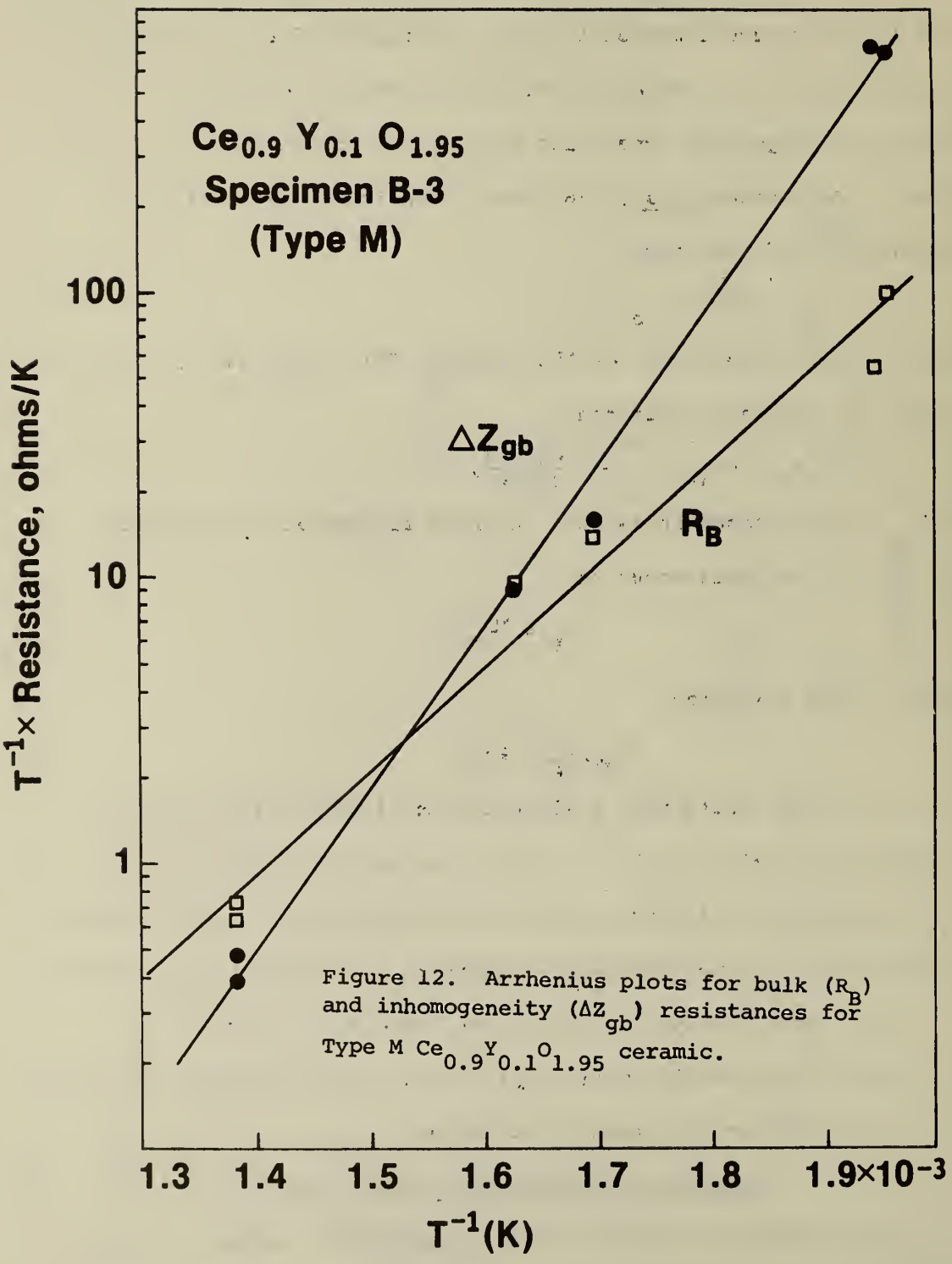

Figure 12. Arrhenius plots for bulk (R_B) and inhomogeneity (ΔZ_{gb}) resistances for Type M $Ce_{0.9}Y_{0.1}O_{1.95}$ ceramic.

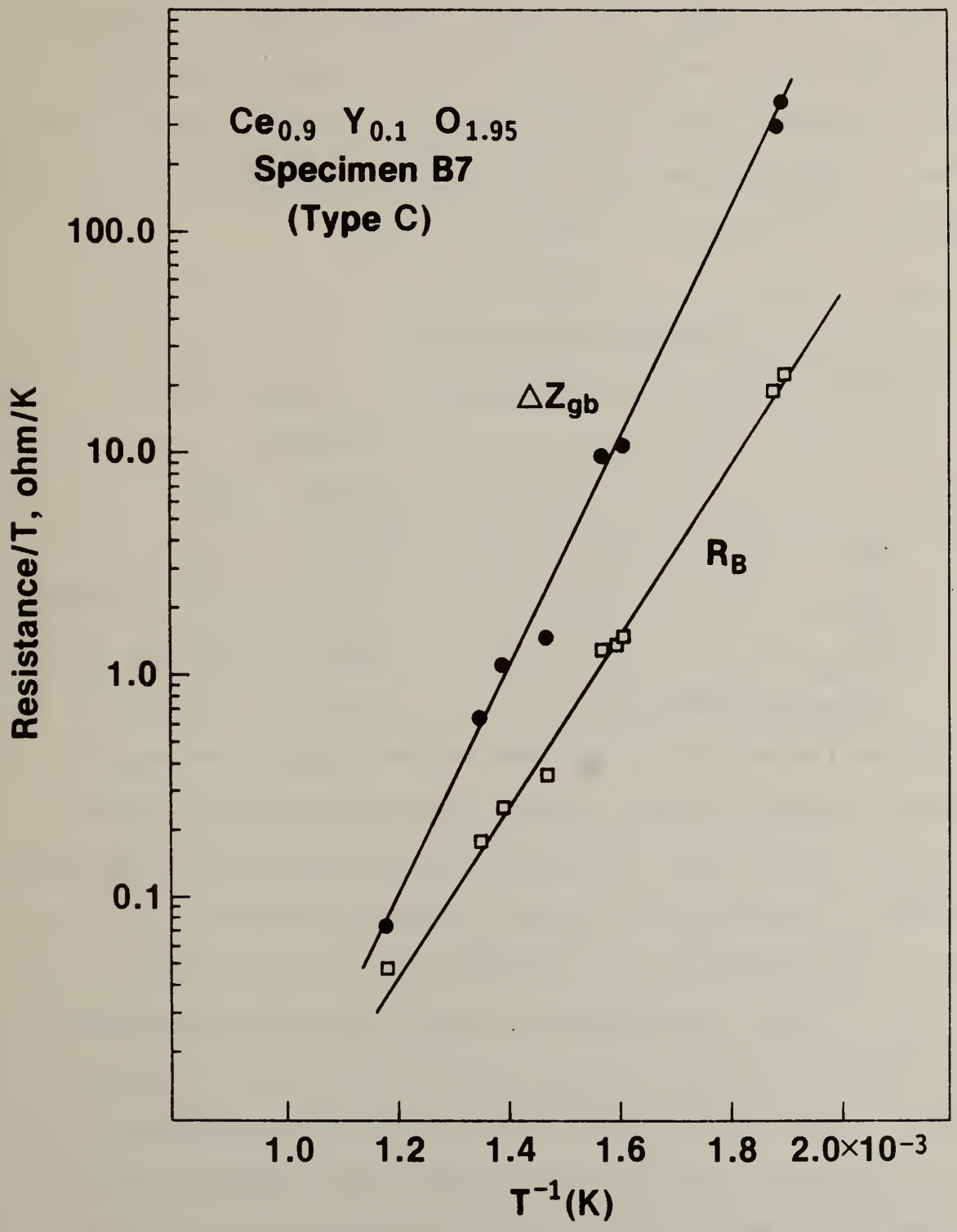

Figure 13. Arrhenius plots for bulk (R_B) and inhomogeneity (ΔZ_{gb}) resistances for Type C $Ce_{0.9}Y_{0.1}O_{1.95}$ ceramic.

the form of plots of $\ell n(R_B/T)$ and $\ell n(\Delta Zgb/T)$ against T^{-1}, where T is the temperature in Kelvin units. Both quantities appear to obey the Arrhenius equation, with greater uncertainty in the Type M specimens because of the overlap of the arcs in the plot of impedance in the complex plane (cf Fig. 9).

The activation energies drawn from least-squares fits to the data in Figs. 12 and 13 are given in Table 5.

Table 5

Activation Energies at Low Temperature for Types M and C Specimens of Y_2O_3-Doped CeO_2

	Specimen B-3	Specimen B-7
Type	M	C
ΔE_{R_B}	69.0±4.9	72.7±1.5 kJ/mole
$\Delta E_{\Delta Z_{gb}}$	108±3.6	98.0±1.9 kJ/mole
Cross-over Temperature	380 °C	790 °C

For R_B the activation energies are close, and the Student's t-value is 2.15 with 14 degrees of freedom, implying that they may not be different at the 95% confidence level. The values of the activation energy for ΔZ_{gb} produce a t-value of 6.54, and they clearly are different.

For each specimen the total dc resistance in a 4-probe experiment would be controlled at low temperatures by ΔZ_{gb} and at high temperatures by R_B. The cross-over point for each specimen is given in the last row of Table 5. These data, and the existence of the cross-over between bulk and inhomogeneity values are very similar to the findings of Kudo and Obayashi [13], whose dc conductivity measurements show bends in the plots of $\ell n\sigma$ vs T^{-1}, with straight-line portions above and below the bend. The activation energies in Table 5 are very similar to their high

and low temperature values. According to the interpretation offered here, then, only the high temperature data, above the bend, represents the true intrinsic properties of the material. The low temperature data reflect the inhomogeneities, presumably grain-boundaries. Similar conclusions were reached by Chu and Seitz [29] for Ca-doped ZrO_2.

Slow Transients

We have begun examining 4-probe resistivity measurements in these materials. Figure 14 is a schematic diagram of the type of sample used. The dc electrical conductivity was measured from 180 °C to 1200 °C. The sample dimensions were 1.7mm x 1.7mm x 13mm. Electrical contacts were made by using Engelhard #6082 platinum paste and platinum wires. A high ac current (>100μA) was applied through the contacts in air at high temperatures to form porous contacts. A dc current of less than 10μA was used over the whole temperature range. All the contacts were ohmic. The temperature was measured by a pair of Pt-Pt 10% Rh thermocouples placed next to the sample.

As described below, the IR drop in the specimen is given by the instantaneous voltage rise between the potential probes when the current step is applied. Such data for a Type C specimen (CHP-2) are shown in fig. 15. The bend at 930 °C is quite clear, and the upper and lower activation energies are similar to those in Table 5 for R_B and ΔZ_{gb} for Type C material. There appears to be reasonable consistency between the ac and dc measurements at this stage.

When we started the small constant dc current through the sample, a transient effect was observed in addition to regular IR voltage drop. Typical behavior is shown in figs. 16-18. Figure 16 gives a schematic representation of the current and voltage pulses observed at the potential

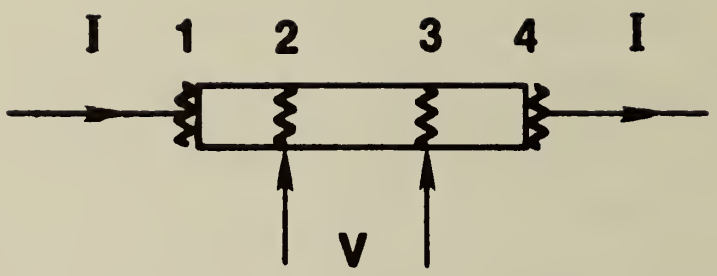

Figure 14. Schematic of 4-probe sample.

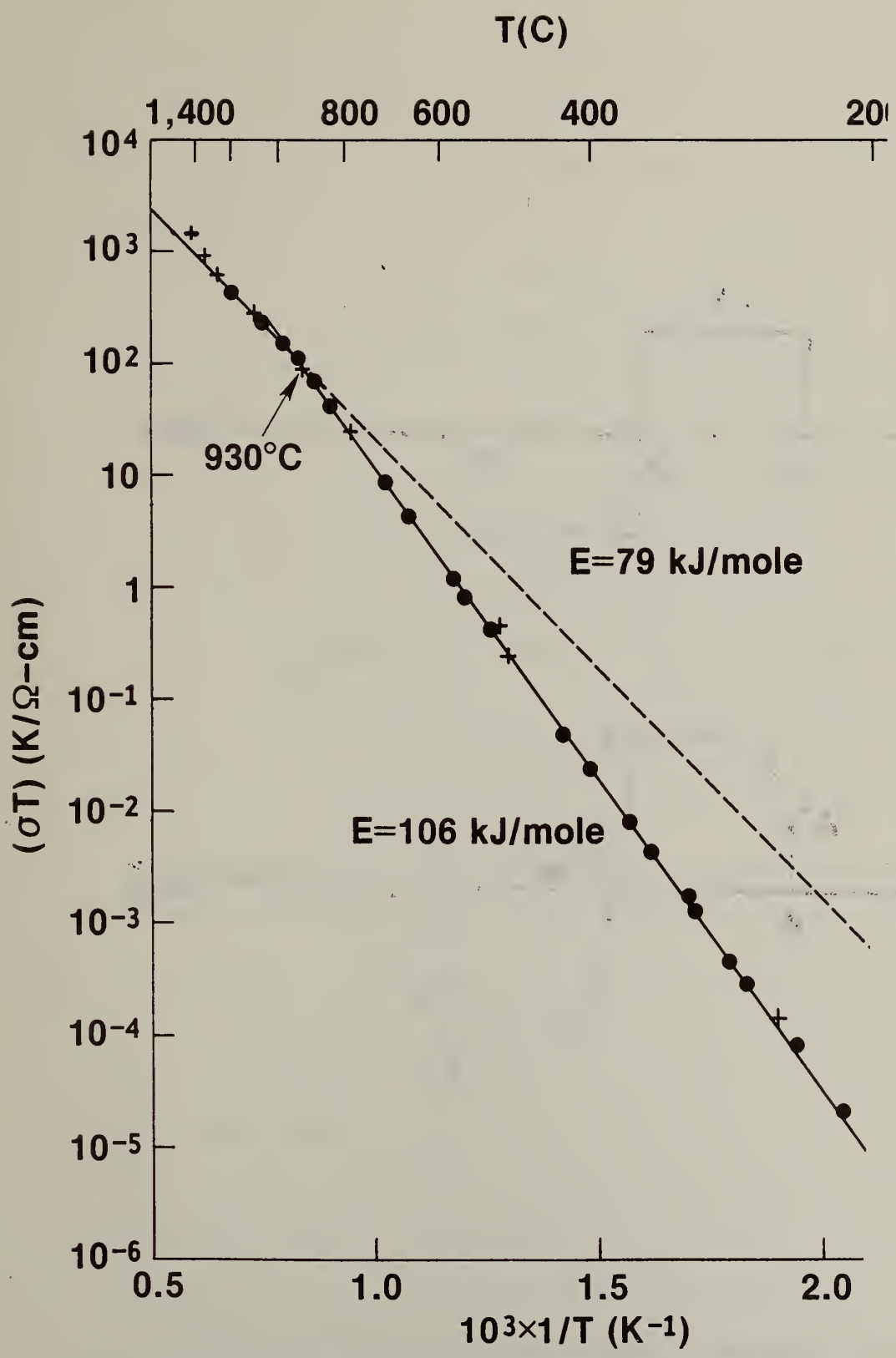

Figure 15. Temperature dependence of 4-probe dc cond
of Type C $Ce_{0.9}Y_{0.1}O_{1.95}$ ceramic in air.
temperatures, and +, failing temperature

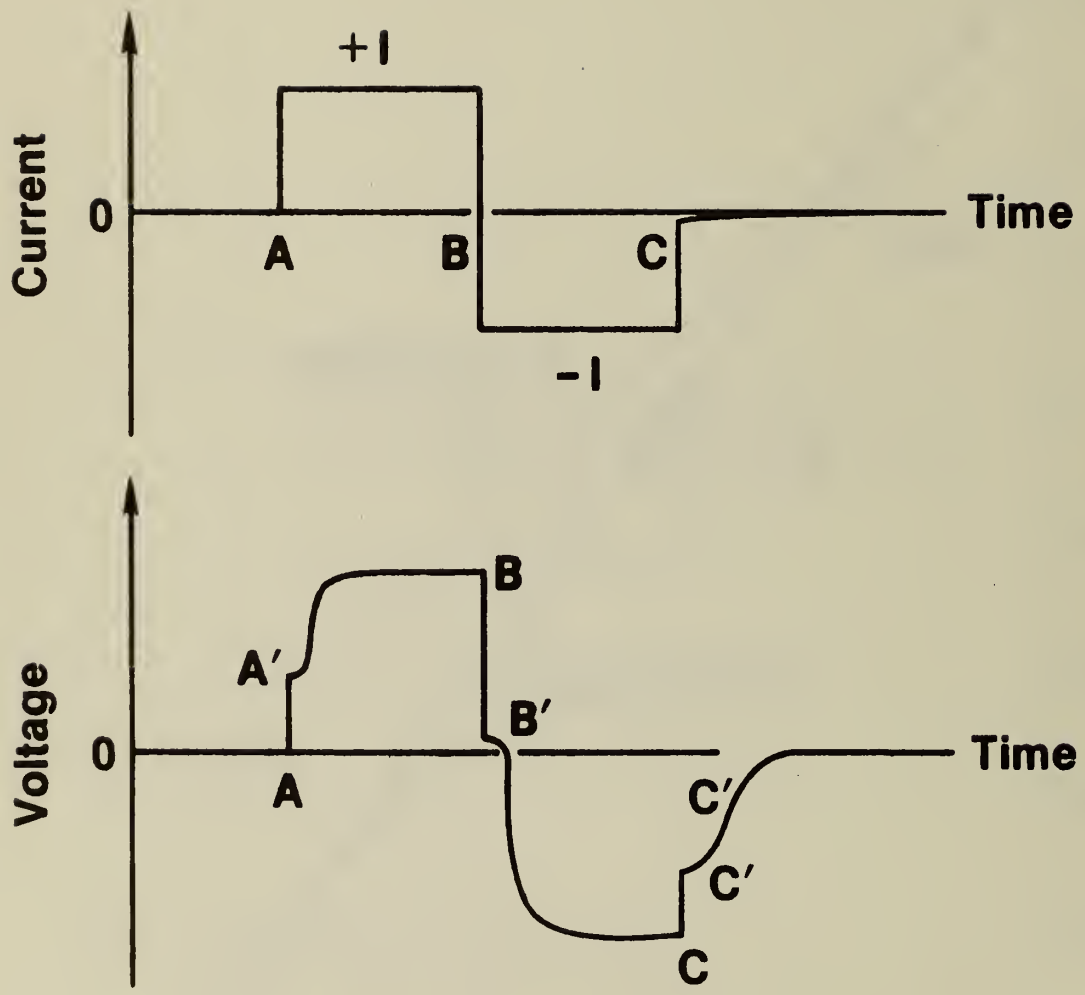

Figure 16. Schematic of current and transient voltage pulses at the potential probes in Type C $Ce_{0.9}Y_{0.1}O_{1.95}$ ceramic.

probes. Four identical electrodes were used as described previously. A constant dc current at the order of 10μA was applied through contacts 1 and 4 (fig. 14), and the voltage response was measured at electrodes 2 and 3. A high-impedance electrometer was used to measure the voltage, so that there was no current drawn at electrodes 2 and 3. Figure 16 shows a typical test cycle of applied current as function of time. The corresponding measured voltage is shown also. Immediately after the current is turned on, there appears the IR voltage, AA'. The transient voltage follows the IR voltage after a short delay time. Figure 17 shows the recorder trace of such a transient, with its delay, on an expanded time scale. The transient voltage increases with time in an S-shaped curve, and finally saturates. Figure 18 shows the recorder trace of one of these transition voltage pulses at longer times. If one reverses the applied current, the IR voltage, BB' (fig. 16) equals twice AA' as expected. The transient voltage also reversed. The effect is symmetrical with respect to the zero current axis. At time C, if one turns off the applied current, the transient voltage relaxes slowly after the IR voltage drop and the delay time as shown in Figure 16.

We shall define the saturation overvoltage V_o as the steady state excess voltage observed in the experiment, excluding the initial IR voltage. Figure 19 shows the relation between V_o and the applied current. The saturation overvoltage is proportional to applied current at low currents, but the curve bends toward lower overvoltages as the current increases. The initial increase of overvoltage with time appears to follow the square root of time. A large linear range can be found in the $t^{1/2}$ plot, as shown in fig. 20. The intercept of the linear line on the time axis indicates the delay time involved in the process.

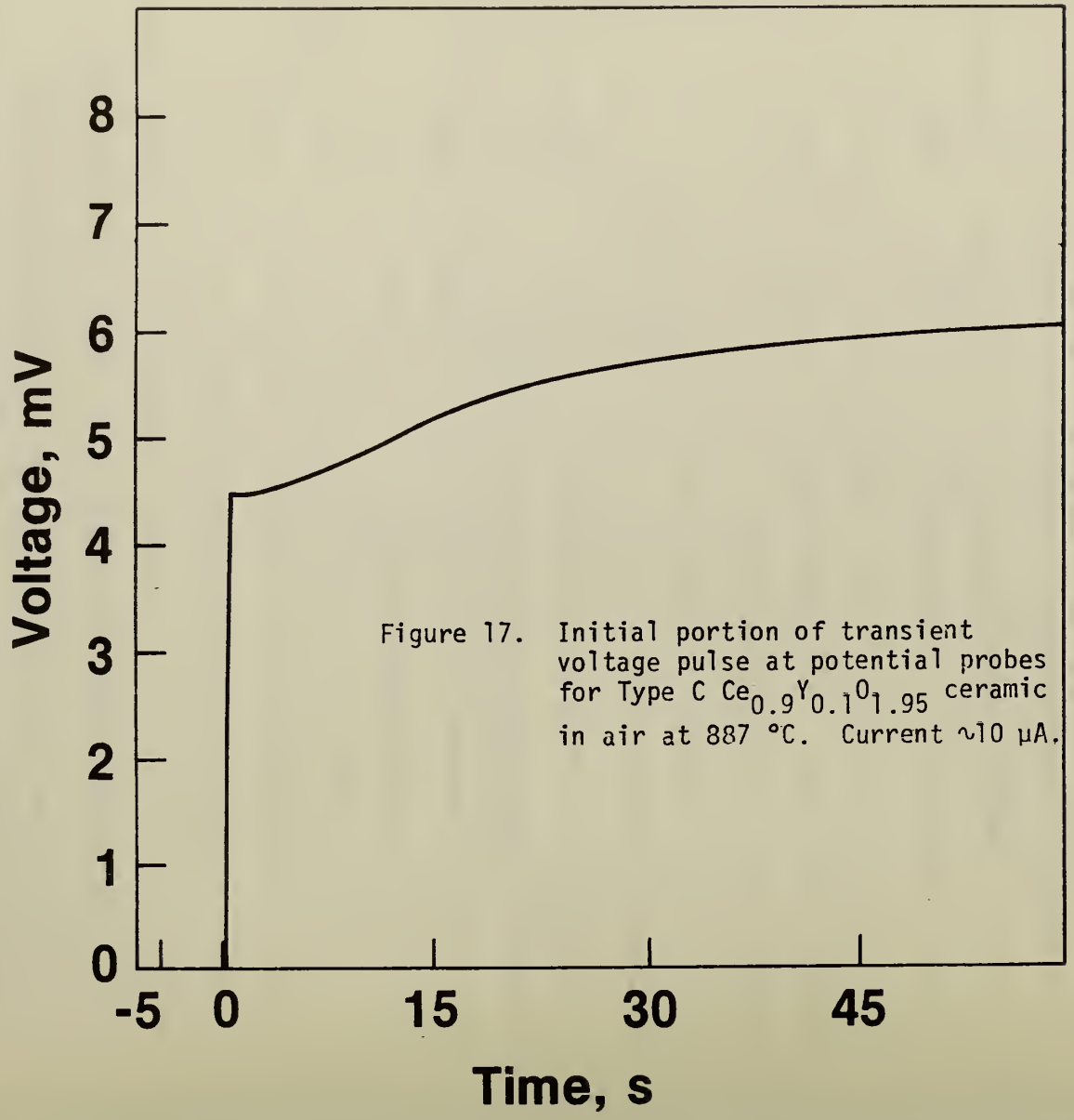

Figure 17. Initial portion of transient voltage pulse at potential probes for Type C $Ce_{0.9}Y_{0.1}O_{1.95}$ ceramic in air at 887 °C. Current ~10 μA.

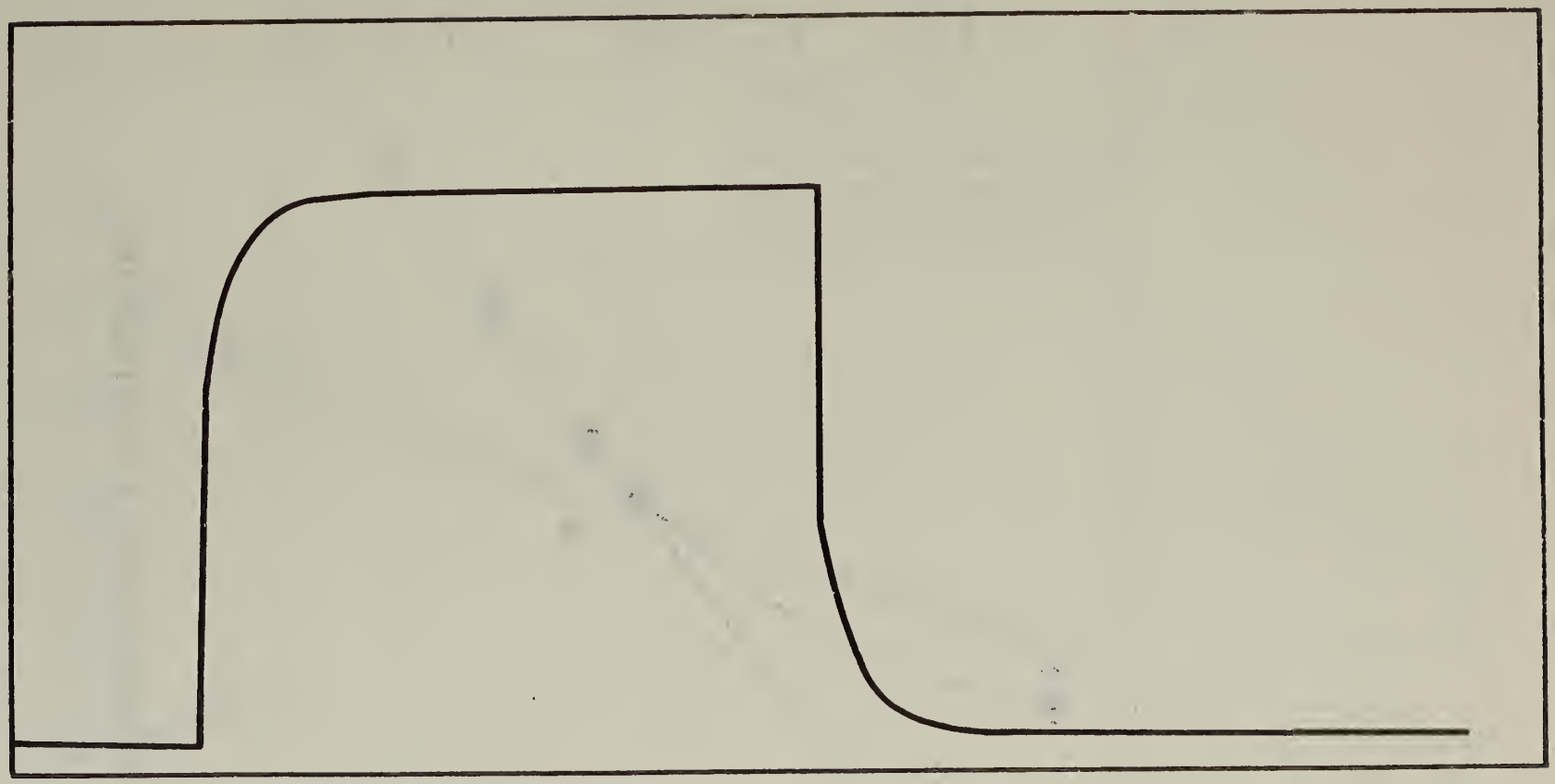

Figure 18. Transient voltage pulse at potential probes for Type C $Ce_{0.9}Y_{0.1}O_{1.95}$ ceramic in air at 887 °C. Current ∿10 μA.

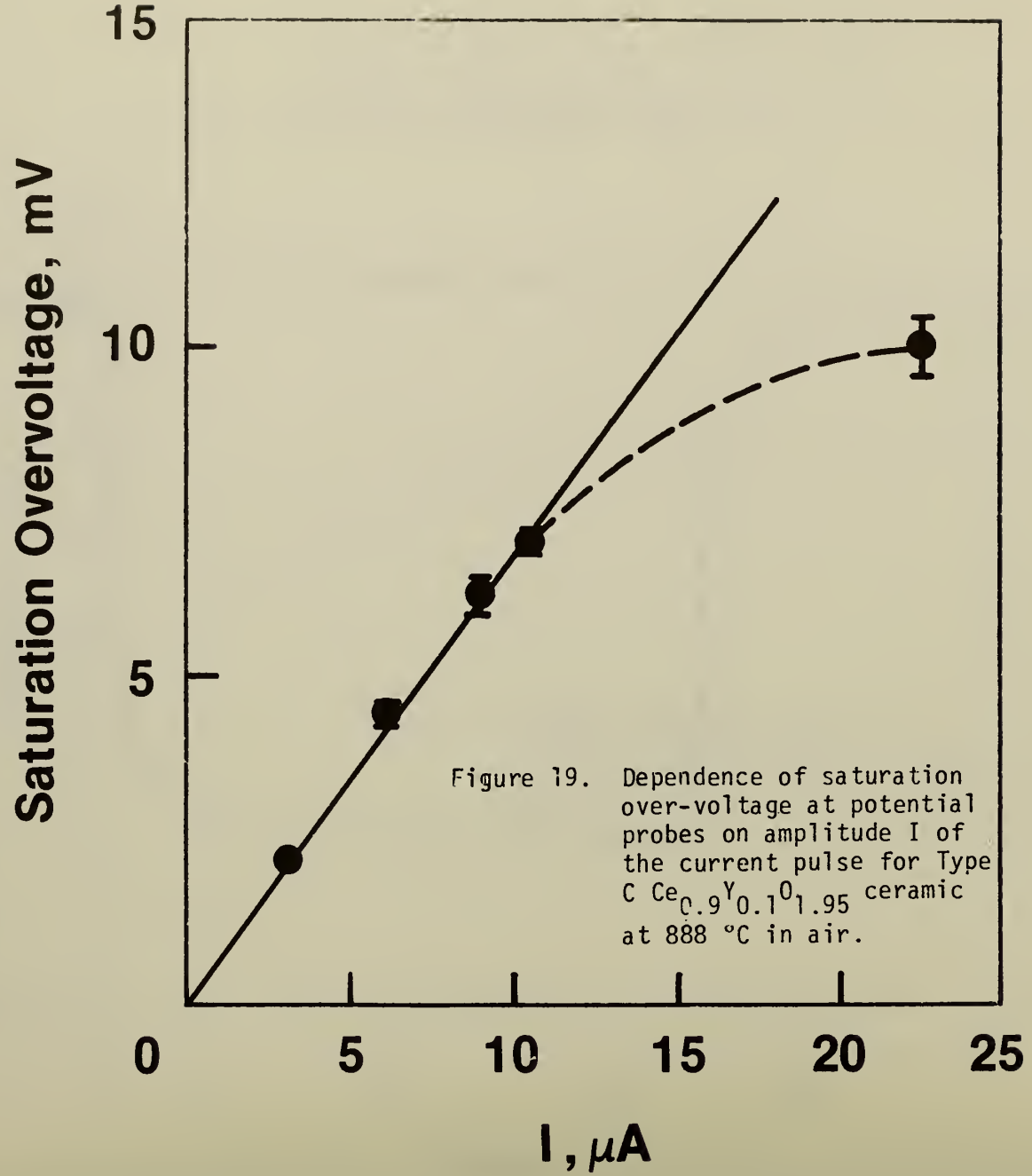

Figure 19. Dependence of saturation over-voltage at potential probes on amplitude I of the current pulse for Type C $Ce_{0.9}Y_{0.1}O_{1.95}$ ceramic at 888 °C in air.

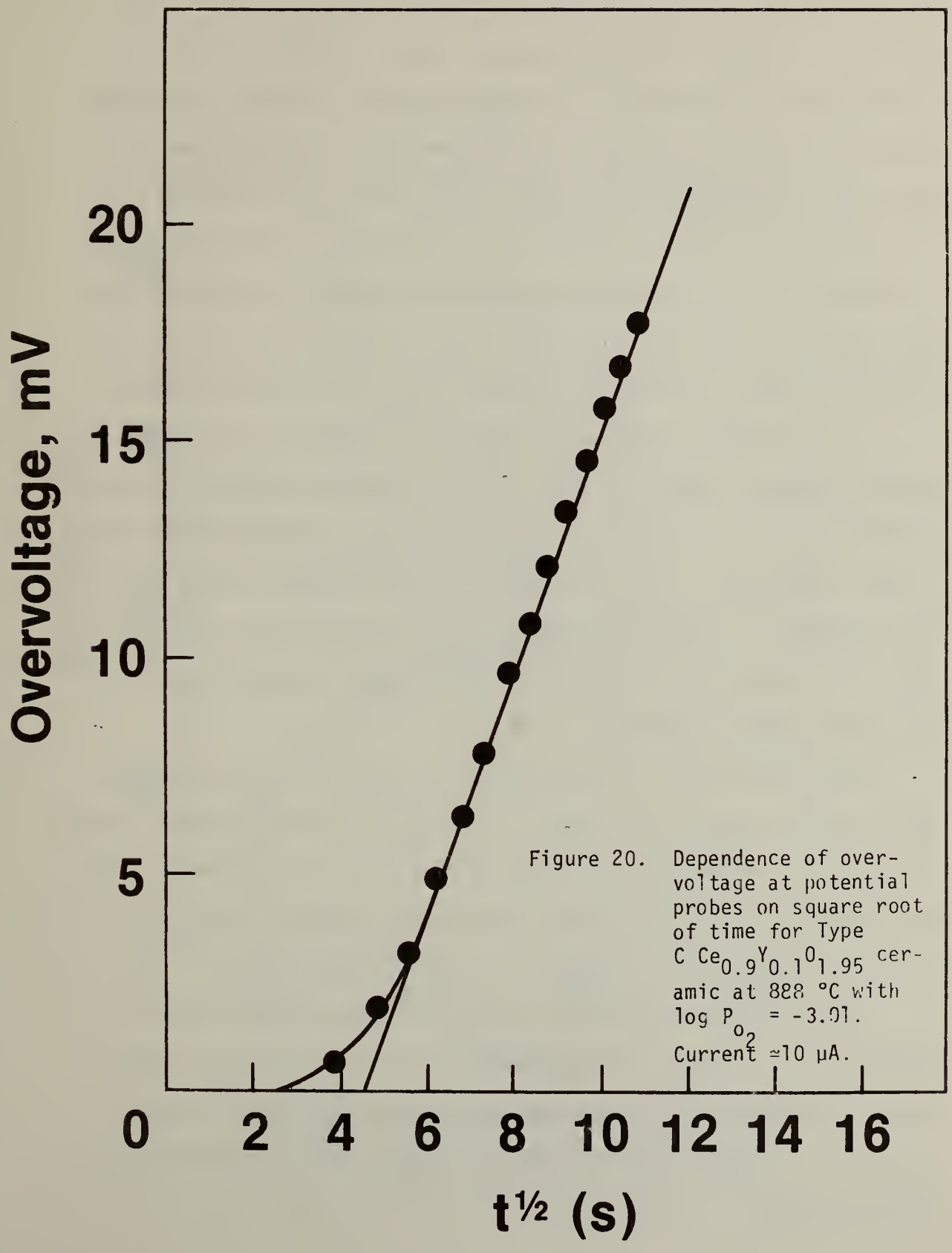

Figure 20. Dependence of overvoltage at potential probes on square root of time for Type C $Ce_{0.9}Y_{0.1}O_{1.95}$ ceramic at 888 °C with log P_{O_2} = -3.91. Current ≈10 μA.

At long times the rate of increase in the overvoltage is reduced and finally the steady value V_o is reached. This overvoltage behavior is different from that observed at a current-carrying (active) electrode. A typical rise in overvoltage observed when the active electrodes are at the ends of the specimen (positions 1 and 4, Fig. 16) is shown in fig. 21, and when the active electrodes are at positions 2 and 3 the rise is as shown in Fig. 22. In both cases there is no delay, so that the time dependence curve is smooth as shown. Note, however, that the rise is slower when there is greater separation between the active electrodes.

The overvoltage V_o was also studied as a function of the oxygen partial pressure. Figure 23 shows the oxygen partial pressure dependence of the saturation overvoltage. The ambient oxygen partial pressure has a large effect on V_o. The IR voltages V_i are also shown in the graph for comparison. As shown in fig. 23 at high oxygen partial pressures V_o and V_i are comparable. However, the overvoltage V_o became dominant at low oxygen partial pressures.

The initial rise of the overvoltage in the $t^{1/2}$ plot also depends on the partial pressure of oxygen. The slopes obtained from plots such as fig. 20 at different partial pressures of oxygen are plotted in log-log form in fig. 24. A straight line of slope between 1/2 and 1/3 appears to describe the data at least down to -log P_{O_2} 2.

The temperature dependence of the delay time was also studied, defined as the time when the recorded voltage at the potential probes starts to deviate from the constant IR voltage. The result is shown in fig. 25. A straight line of activation energy 80.1 kJ/mol describes the data quite well.

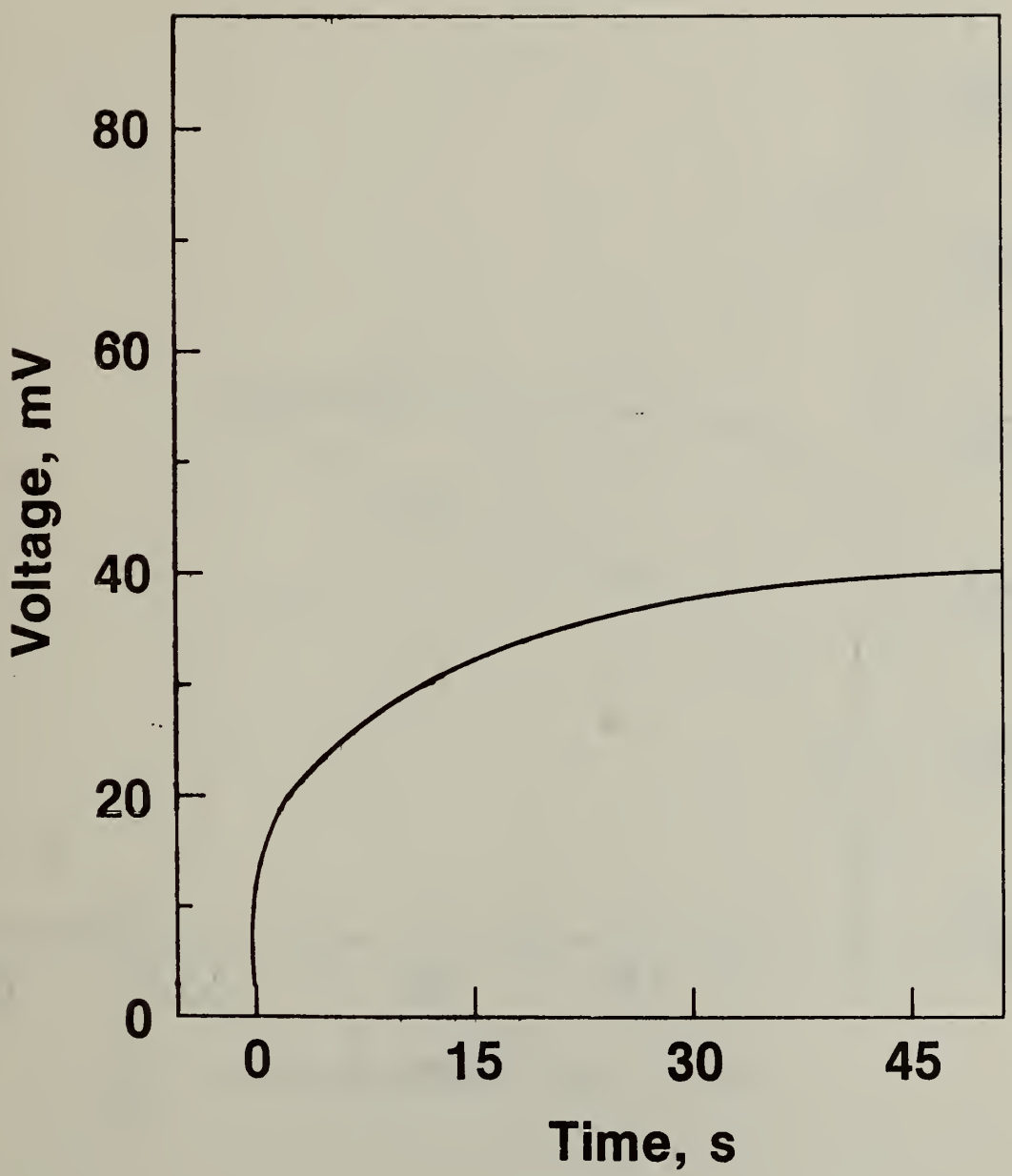

Figure 21. Transient voltage pulse on active electrodes, placed at ends of specimen, for Type C $Ce_{0.9}Y_{0.1}O_{1.95}$ ceramic at 888 °C in air. Current ≈10 μA.

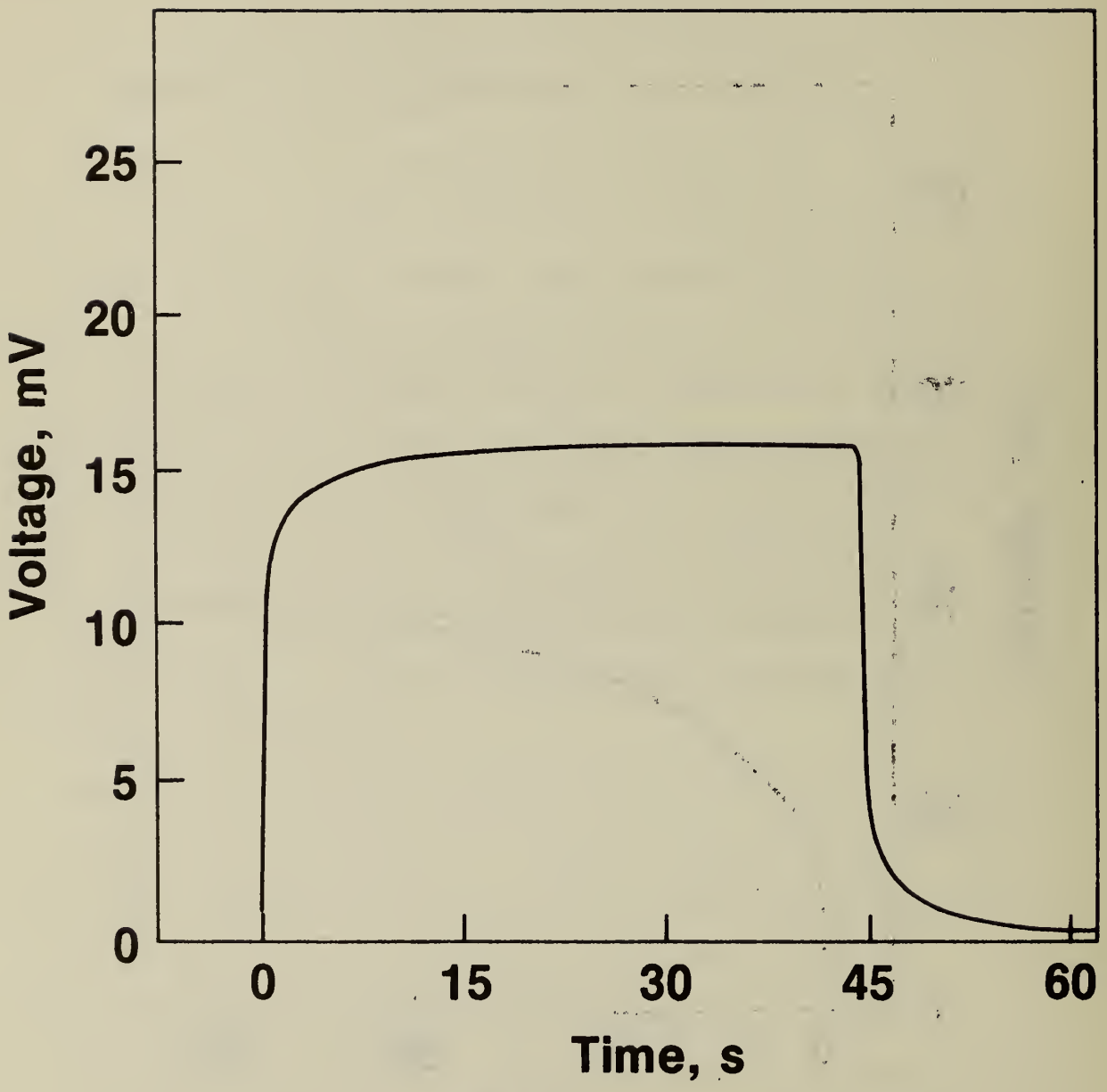

Figure 22. Transient voltage pulse on potential probes used as active electrodes for Type C $Ce_{0.9}Y_{0.1}O_{1.95}$ ceramic at 887 °C in air. Current ≃10 μA.

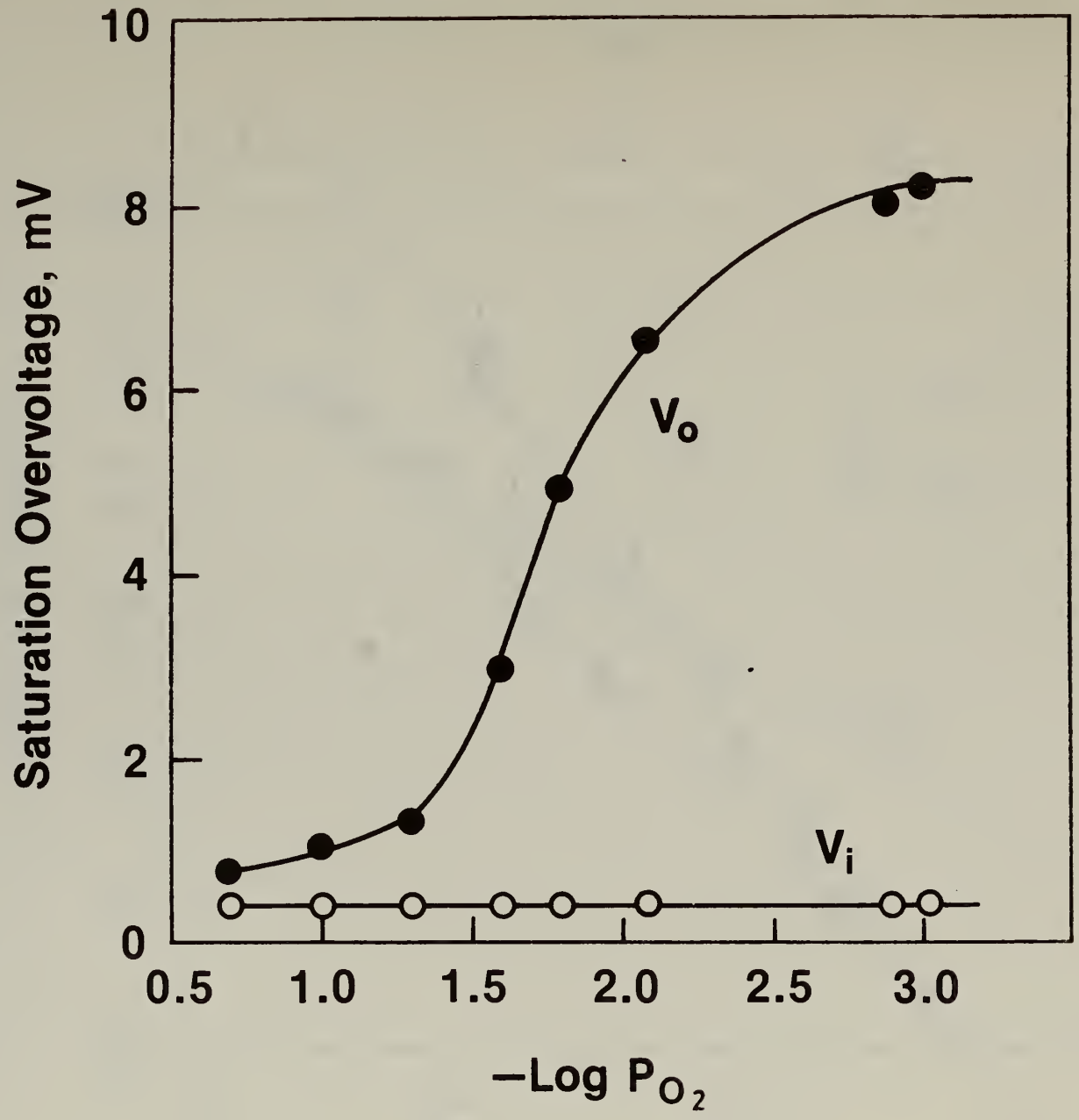

Figure 13. Dependence of saturation overvoltage at potential probes on oxygen activity for Type C $Ce_{0.9}Y_{0.1}O_{1.95}$ ceramic at 888 °C. Current ±10 μA.

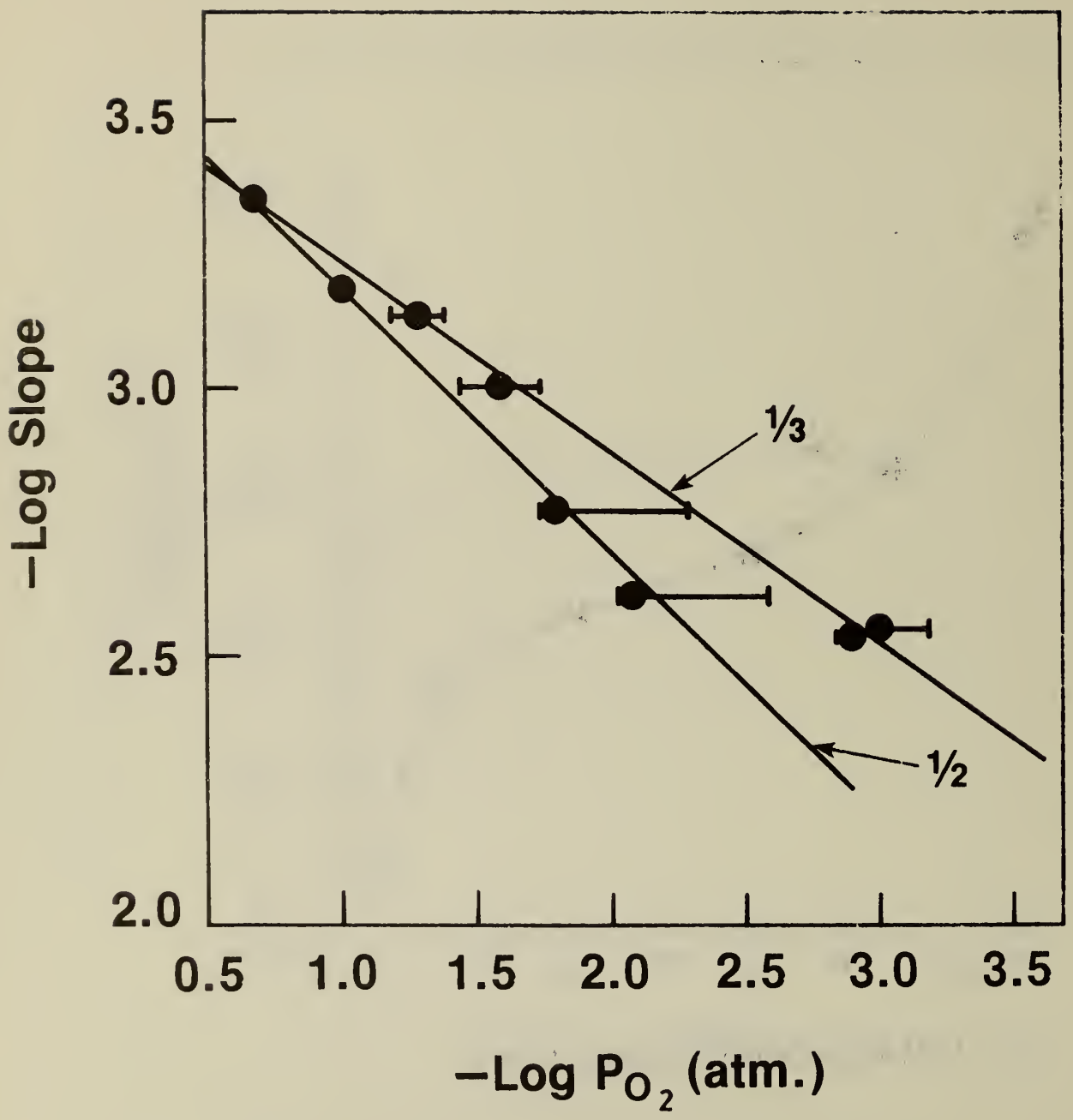

Figure 24. Dependence of the slope of the $t^{1/2}$ plot on oxygen activity for Type C $Ce_{0.9}Y_{0.1}O_{1.95}$ ceramic at 888 °C. Current ≈10 μA.

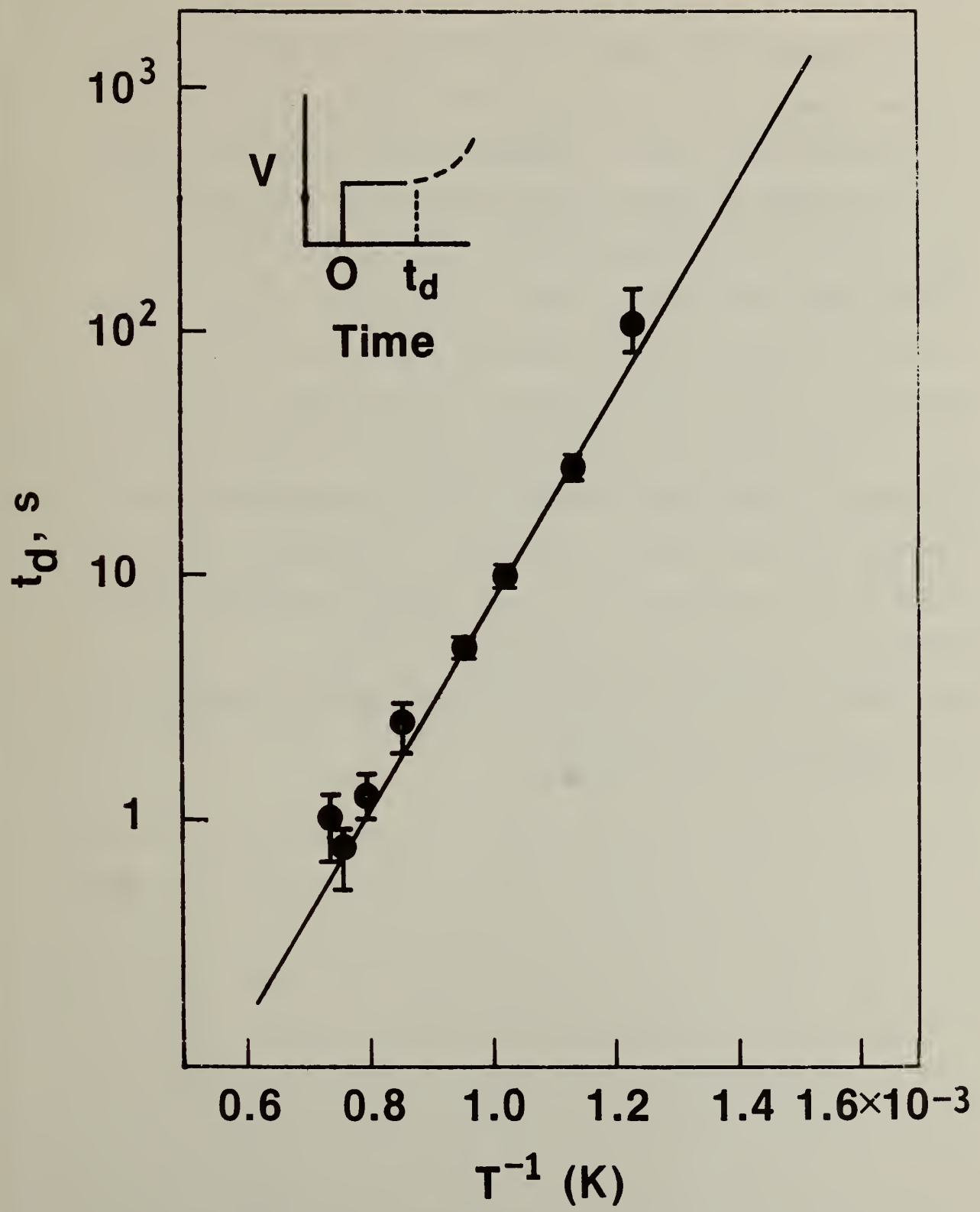

Figure 25. Arrhenius plot for delay time for Type C $Ce_{0.9}Y_{1.0}O_{1.95}$ ceramic in air. Current ~10 μA.

This transient effect appears to be governed by a diffusion process involving diffusion in the solid state. This fits the initial $t^{1/2}$ behavior seen in fig. 20 and the Arrhenius behavior of the delay time in fig. 25, for which the activation energy is very like those of the oxygen transport processes observed in the bulk through R_B and ΔZ_{gb}. It further agrees with the fact, shown by a comparison of figs. 21 and 22, that the rise time at active electrodes depends upon the distance between them. We are currently examining a model suggested by Fouletier et al. [30] to account for oxygen semi-permeability in stabilized zirconia, and recently invoked by Wang and Nowick [31] in somewhat modified form to account for similar effects in doped CeO_2. In this model, some of the oxygen flux represented by the steady current is supplied by coupled diffusion of electrons and oxygen vacancies. We believe this may be taking place primarily in the grain boundaries, and plan to study the effect intensively in the near future.

2.3 Automated Electrochemical Measurement System

Introduction

Experiences with operation of our system [32] and proposals for use of the system in pulse measurement have resulted in several modifications of the original instrument. A need for additional programming has also become evident, over and above that necessary for operating the modifications. The bulk of this section of the report is concerned with discussion of these facts and the resulting designs. For convenience, this discussion will be separated into three parts. This procedure will be followed since each part can stand alone even though it has been derived from consideration of relationships with the others. These interconnections will be indicated where necessary.

2.3.1 Mass Storage

Very early in the operational history of the instrument, it became obvious that mass storage of some kind was a needed adjunct. As an example of the need, consider the situation where we are repetitively performing an electrodynamic scan of electrode characteristics. We would like to be able to examine the data from each scan as well as the average of all scans. Depending upon scan speed, we can either print each run or store each run. If the scan speed is too fast, we can only store each run. Because of memory capacity limitations, in the original system we summed each run with the previous ones. This allowed us to look only at the average of all scans unless we could slow the scan rate enough to allow printout of each scan.

Several approaches can be utilized to resolve this problem. All are some kind of enlargement of the original memory. First we could just enlarge the memory capacity of the instrument. This is relatively

expensive and subject to loss of data on a power-failure. Second, we could store each scan on a magnetic tape cassette. We are limited here by the speed of data transfer to tape [in the present arrangement a maximum of 120 characters (bytes) per second], and by the fact that cassette storage is sequential and therefore data retrieval is slow. A third approach is to use "Floppy Disc" storage. As in the case of cassette storage, data is sequentially-stored. However, we can access a particular block of data directly without going through an operation that passes all preceding data through the system as in a cassette system. Data transfer is rapid going at speeds up to about 3×10^4 characters per second. This last approach was the one selected.

There are a large number of Floppy Disc units available, and therefore, we must establish specifications for selection. The criteria we established were:

(a) In order to minimize software overhead and interfacing, the unit selected must have a controller built in.

(b) For compatibility with other existing NBS equipment, the disc should be single-sided, 8", single density and the recording format should be IBM-3740 compatible [33].

(c) There should be a minimum of two drives, all operated by the same controller.

(d) Data transfer between the disc unit and the instrument should have the option of either direct transfer at maximum speed or on a single byte basis under command of the instrument CPU.

A Floppy disc unit meeting these specifications has been purchased. It has resident microprocessor control and includes a 1024 character buffer memory. Two sets of commands are operable (Table 6). One involves

direct transfer of data between disc and CPU while the other operates through the buffer on a character by character basis.

Table 6

Summary of Floppy Disc Unit Commands

Command	Code per characters	Data Flow	Data Transfer Control
Bootstrap	00	Disc to Host (CPU)	DMAC*
Read Status	01	Disc to Host	CPU
Read Auxiliary Status	02	Disc to Host	CPU
Load Sector Count	03	Host to Disc	CPU
Read Last Access	04	Disc to Host	CPU
Read Data	05	Disc to Host	DMAC
Write Data	06	Host to Disc	DMAC
Read Buffered Data	07	Disc to Host	CPU
Write Buffered Data	08	Host to Disc	CPU
Write Deleted Data	09	Host to Disc	DMAC
Write Deleted Data Buffered	0A	Host to Disc	CPU
Copy Date	0B	Disc to Disc	---
Initialize Indexed**	0C	Host to Disc	CPU
Initialize**	0D	Host to Disc	CPU

*DMAC (Direct Memory Access Controller).

**Initialize differs from Initialize Indexed in that Initialize formats all tracks the same whereas Initialize Indexed formats track 00 in 26 sector IBM format and the rest of the tracks in the format specified with the command.

Interfacing of the disc unit to the potentiostat control requires (as a minimum) only a single parallel peripheral Interface adaptor (PIA), and some bus transceivers (fig. 26a). At a clock rate of 1 MHz, the PIA programming to write (or read) one byte of data to (or from) the disc unit takes an absolute minimum of 32 μs, a time which corresponds to the maximum data transfer rate of the disc unit (31,500 characters per second). There is no margin for error. However, Direct Memory Access (DMA) was already being considered for a high speed data acquisition board, and an interface for the disc unit using this method is also relatively simple (fig. 26b). The only problem here is that the instrument clock requires modification. This difficulty is easily surmounted by the use of a commercial clock module [34] which is already configured for this use. Figure 27 shows the resulting modification.

The interface that we have designed (fig. 28) is capable of operation in either of the above modes. [Table 6 includes a column which indicates the planned mode for each disc command]. This system (interface, power supplies, disc unit) has been assembled. Some of the needed programming has been done, and the combination is presently being debugged. When fully programmed and checked out, this interface will allow us to select (in software) either of the two modes of operation. It should be noted here that the DMA controller chip (6844) allows three modes of DMA. One of these modes stretches the clock period and does not halt the CPU. The other two modes both halt the processor, one for the time necessary to transfer an entire data block and the other for the time needed for one character. Transfer speed can be as fast as the basic CPU clock (921.6 KHz in this case). It should also be noted that the new clock circuit replaces the Band Rate Generator clock as well, and provides for the use of Dynamic memory circuits if desired.

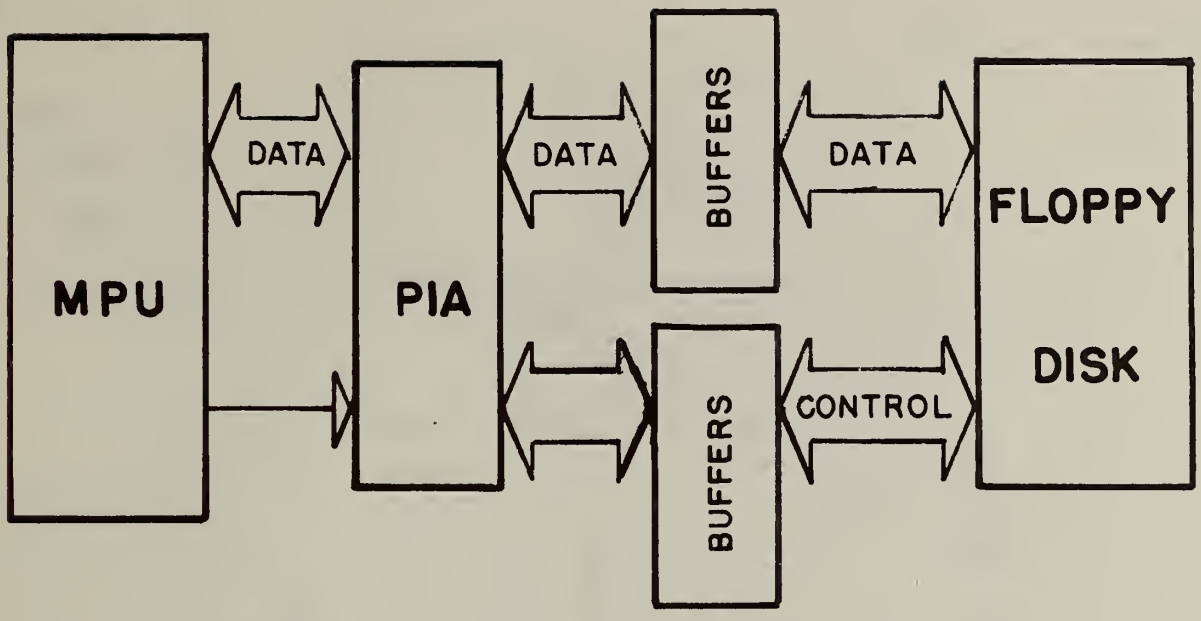

Figure 26a. Block diagram of PIA based interface for Floppy disc.

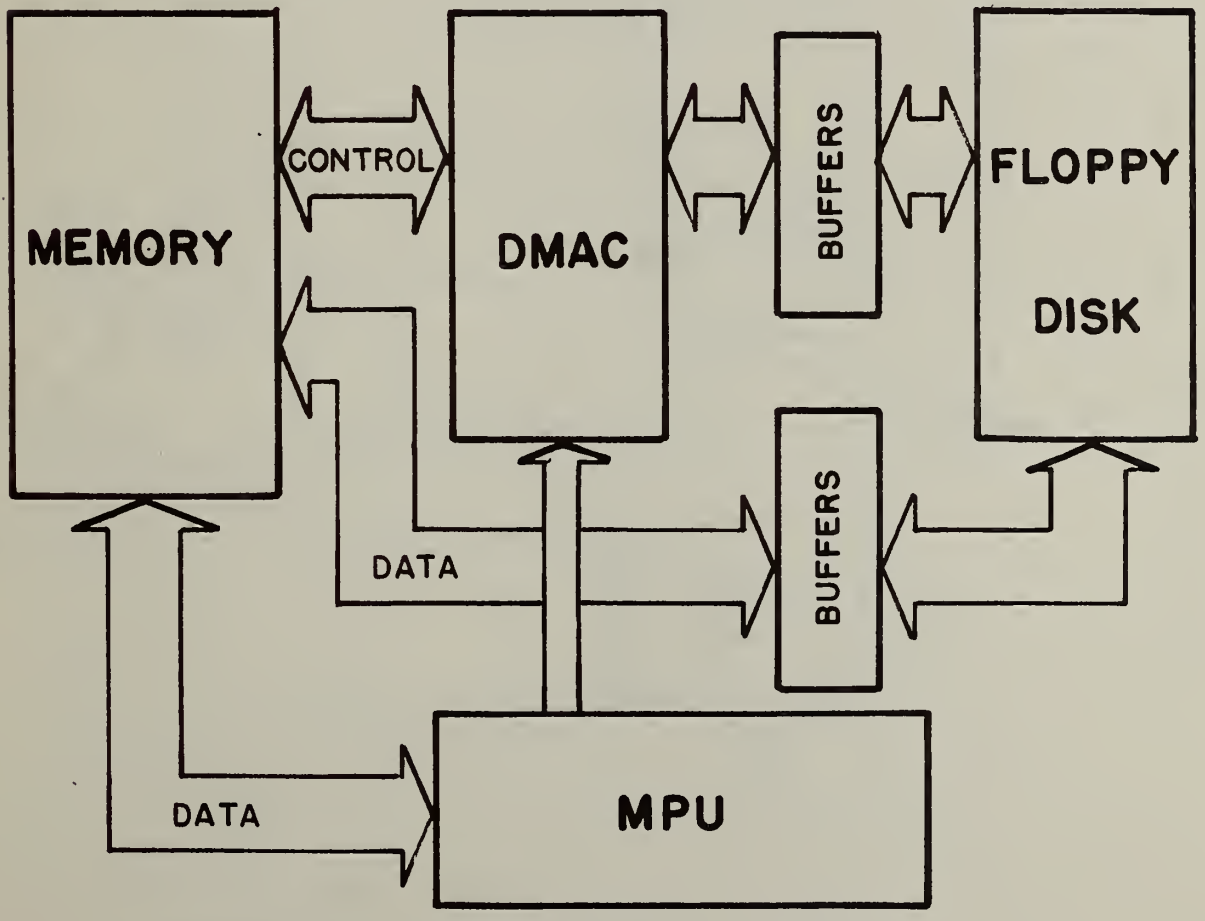

Figure 26b. Block diagram of Tracking Type ADC.

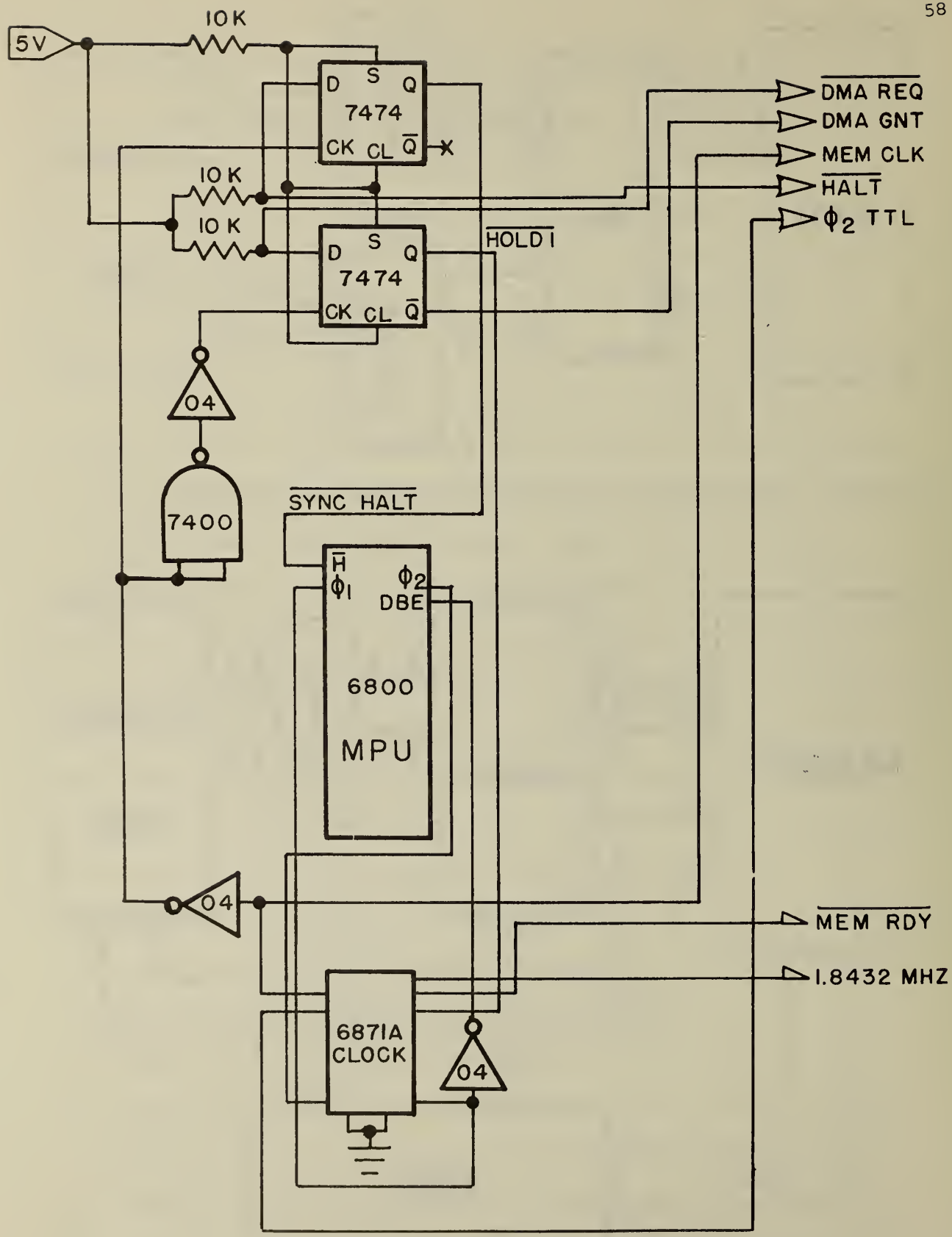

Figure 27. Modified clock circuit utilizing Integrated Crystal Controlled clock.

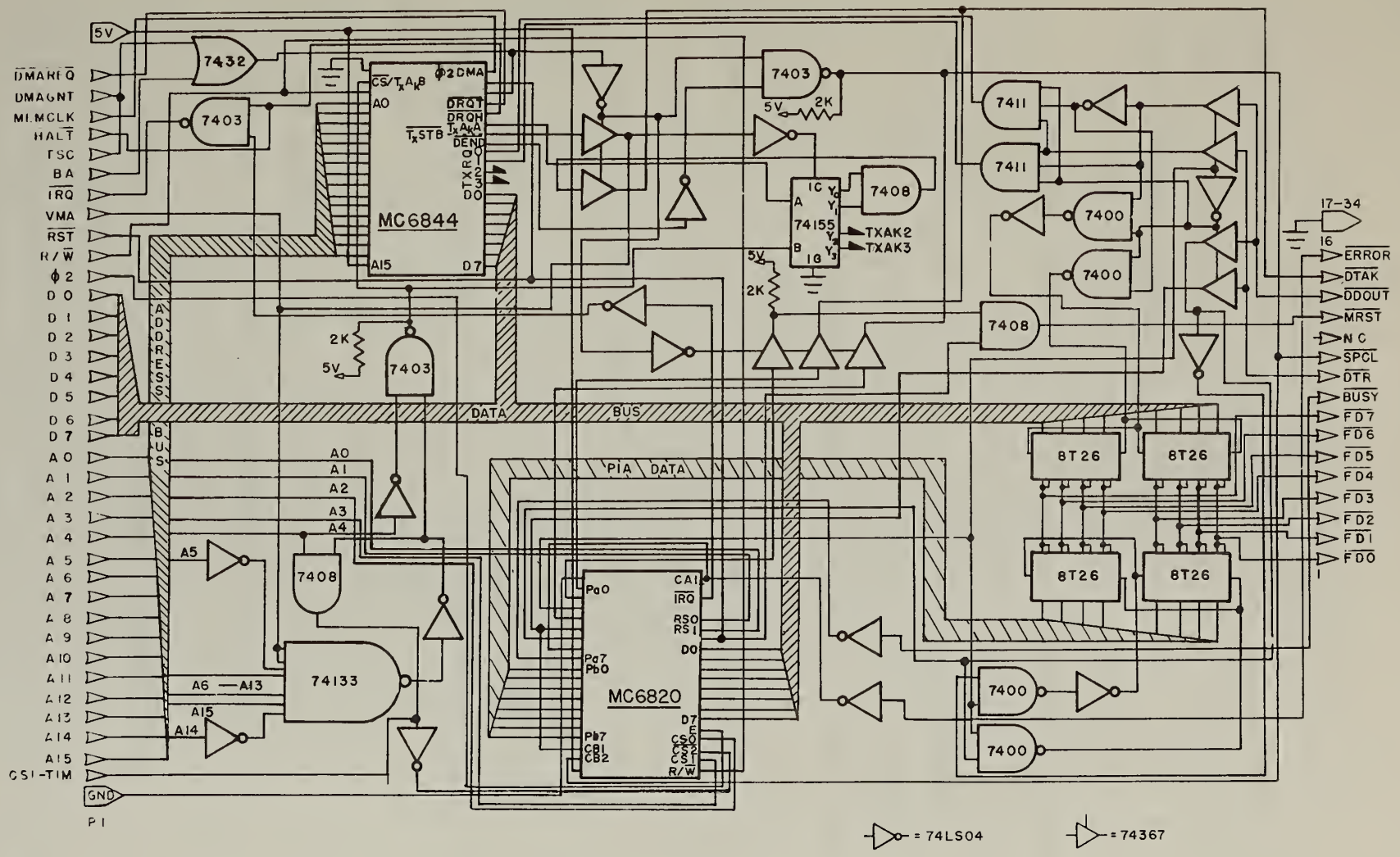

Figure 28. Schematic diagram of complete Floppy Disc Interface

2.3.2 High Speed 12-Bit Data Acquisition System

Experimental usage of the Microprocessor-controlled Electrochemical Measurement System has exposed some drawbacks in the design of the data acquisition board. These restrictions appear only when maximum sensitivity at high speed is desired. However, for pulse mode operations, these limitations are severe difficulties. In the subsequent discussion, these restrictions will be examined and their solutions delineated in terms of a general overview of digital production and measurement of analog quantities. Prior to this, however, some general concerns of Input-Output (I/O) to the data system must be expressed.

Experience has demonstrated that several aspects of I/O connection between the system and the experiment need revision. First, the addition of overvoltage (or overcurrent) protection circuitry for all inputs and outputs is required. Although there have been no difficulties due to inadequate protection, the possibility does exist. We must also provide some fixed level input-output lines (logic lines) to be used for control functions such as relay operation, limit switch detection or interrupt lines. All such lines should be maskable by the CPU so that their functions can be disabled without interfering with system operation.

Access to the data system should be via memory-management techniques. By this is meant that the Data Acquisition System is to be treated as a set of memory locations, and all control instructions, data input, and data output are performed as normal memory accesses from the microprocessor supervised by the usual program instructions. This technique simplifies programming and allows for high speed operation both by normal procedures and by DMA. This implies, of course, that the data system must be, to a

certain extent, self controlled. That is, it must be capable of operating alone upon receipt of the appropriate instructions and parameters from the microprocessor (μP). Also, it must generate status signals indicating what state it is in, when queried by the CPU.

The basic parameters governing the performance of a Digital to Analog Converter (DAC) are resolution (number of bits) and settling time [35,36]. This applies to either the straightforward use of the device to generate an analog voltage or to its use as a component part of an Analog to Digital Converter (ADC). The resolution is the smallest analog quantity that can be generated while the settling time is the shortest interval allowed between full scale changes. If we wish to generate a triangular wave of 30 KHz frequency at a resolution of 12 bits with full scale magnitude we find that a settling time of 4 ns is required [33 ms divided by 8192 (2^{12} points up and 2^{12} points down)]. Granting that the settling time for a one bit change will be less than for a full scale change, it is still unrealistic to expect to obtain that performance when we note that available 12 bit DAC's have settling times in the range of 100 ns to 100 μs. However, a square wave of the same parameters with a rise time of 1 μs or less could easily be generated by a large number of available DAC's. This square wave processed by a precision op-amp integrator [37] would yield a triangular wave of the desired parameters. Clearly, we must be prepared to accept variations in signal processing techniques if we wish to accommodate the limitations imposed by the basic parameters of the DAC. In any case, we must optimize these parameters in light of the desired experimental method.

All DAC's exhibit an undesired phenomenon known as a "glitch" [38]. It is an extraneous output pulse generated when the digital input changes state and it is primarily observed when a number of bits change state at the same time (e.g., 01111111 goes to 10000000). The energy contained in this pulse is a function of the number of bits changing state and is proportional to the width of the clock pulse. Thus to minimize the glitch we minimize the clock pulse width. However, the glitch is always there! In low speed applications its influence is small and it can be ignored. In high speed applications, on the other hand, its effects can be serious and we must therefore deal with it. The best technique is to utilize a "sample and hold" [39] device on the DAC output, which delays a change in output until after the effects of the glitch have dissipated. In ADC applications, the deglitching circuitry can be incorporated in the comparator stage design.

The output magnitude of the DAC signal will depend upon the application, and should therefore be controllable by the μP. This may be achieved by the use of a programmable amplifier (or attenuator) on the output. Such a device may be included in the deglitching circuit or may be separate. Irrespective of the need for signal level control, this is a logical location in the design for output protection circuitry, the need for which has previously been discussed. Figure 29 summarizes the DAC design.

High speed ACS's present further problems, which must be resolved, as well as the ones already discussed. These will be considered sequentially from the analog input to the digital output.

The input stage, in addition to the input protection already discussed, must contain filtering. This filter should be a lowpass type and its cutoff frequency should be no greater than that determined by the Nyquist condition [40], in order to reduce "aliasing" [41] problems. This

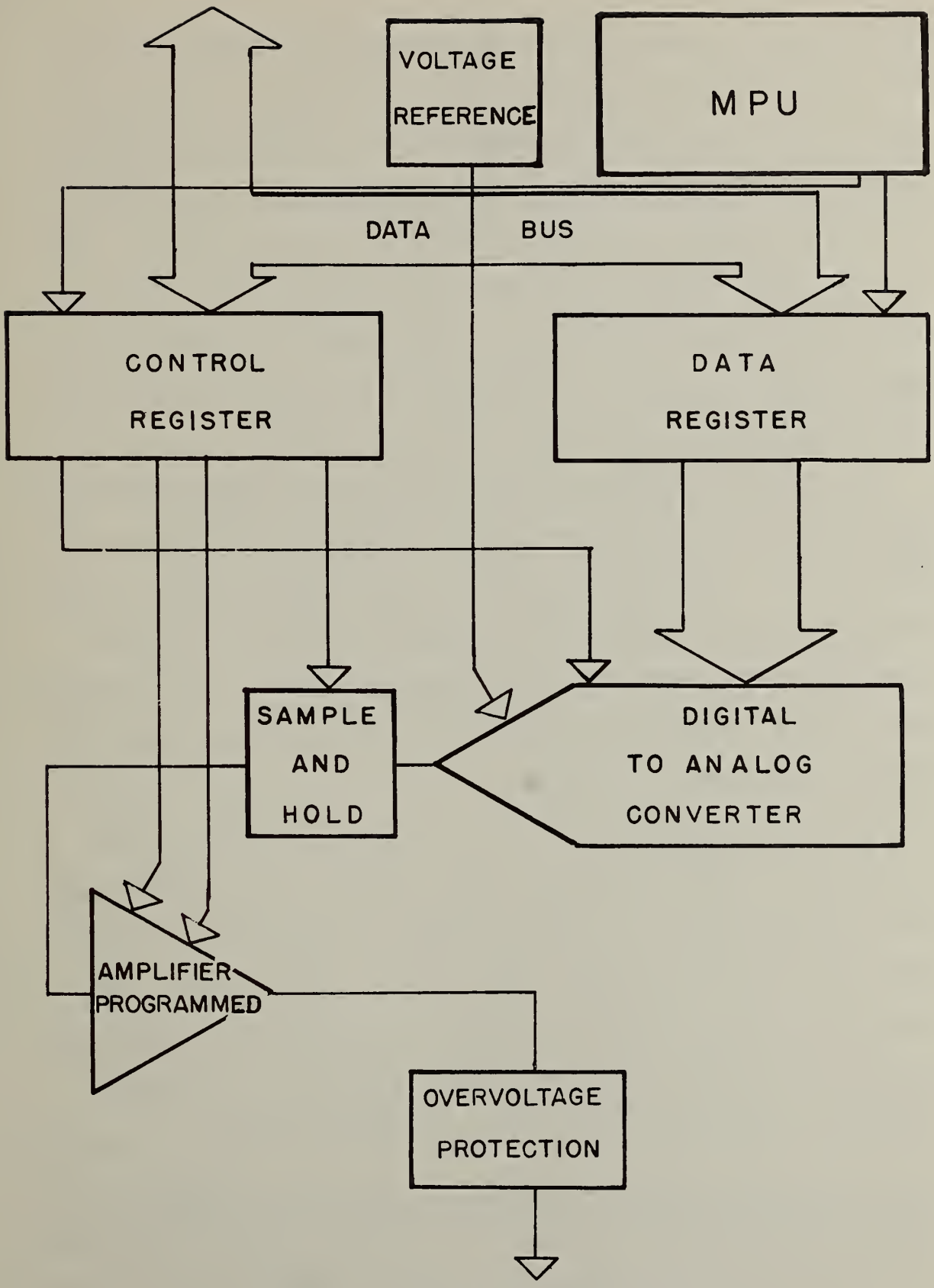

Figure 29. Digital to Analog Converter Block Diagram

frequency will of course be one of the original design parameters and as such enters into the choice of basic DAC characteristics (settling time). Ideally, the filter resonant frequency should be softwave programmable, but manual changes are acceptable. The frequency rolloff of the filter beyond cutoff should be as steep as possible (> 12 dB per octave). This leads to greater complexity of filter design and more susceptibility to error than with simpler filters. Very steep rolloffs are probably best attained with active filters. This implies the possiblity of including signal amplification in the filter section.

The choice of measuring technique governs the next stage configuration. This stage might contain circuits such as absolute value amplifiers [42]; peak detectors, sample and hold circuits, programmable amplifiers [43]; polarity detectors or multiplexers. These functions do not need to be described in detail since their names adequately describe their operation. The discussion of measuring techniques will indicate which of these are needed for each particular method.

The factors that are in control of the type of Analog to Digital converter are primarily conversion speed, precision and flexibility. Of these, conversion time is the most important. Depending upon the regime under investigation, the optimal choice will be either the Successive Approximation [44] or Tracking type* [45]. In either case, consideration must be given to both unipolar and bipolar operation. Determination of which mode is preferable depends upon the desired resolution.

---

*Other conversion techniques will not be considered since they are slower than these two.

At this point, a short discussion of the principle of operation of SA and Tracking type ADC's is worthwhile. Successive Approximation converters operate by a bit by bit comparison of the output of a DAC to the analog input. In other words, the operation consists of a comparison of the input to the output of the DAC with the Most Significant Bit (MSB) set. If the DAC output is lower, the next MSB is set and the comparison repeated. If the DAC is higher, the MSB is cleared and the comparison with the next MSB is performed. This process continues until all bits down to the LSB have been compared. The process takes n + 1 clock cyles where n is the number of bits of resolution that the DAC has. To a first approximation, the time to acquisition is $t_A \leq (n + 1)t_s$ where t_s is the settling time for full scale input [44].

On the other hand, the Tracking type ADC uses an up/down counter for the source of the digital input to the DAC. The count direction is set by the output of a comparator whose inputs are the DAC output and the analog voltage being measured. The counter always operates so that at match the DAC output "dithers" ± 1 LSB. The time for acquisition is thus given by $t_A \leq nt_S$ where n in this case is the number of counts needed to match the input voltage. Since we are concerned here with changes on the scale of one LSB at a time, the actual t_S to use is considerably less than that t_S required for a full scale change [45].

Comparison of the two types shows that there are basically 2 distinct aspects to consider. First, as regards precision, the Tracking type ADC always "dithers" ± 1 LSB. The Successive Approximation ADC gives a fixed answer for each conversion. The precision of this value however will also vary ± 1/2 LSB. Another way of stating this comparison is that the Tracking type makes a conversion per clock pulse with a precision of ± 1 LSB while the SA makes a conversion every n + 1 clock pulses with a precision of ± 1/2 LSB.

The second aspect to consider is speed. The conversion time for an SA-ADC is the same regardless of the magnitude of the analog input change. Thus for input changes greater than $\sim(n + 1)$ LSB's the Tracking type is faster. Thus the choice of type of ADC depends on the magnitude of the "instantaneous" change in analog input.

Table 7 and fig. 30 are comparisons of these two types indicating the accessory devices needed, as well. This comparison shows that consideration of some sort of hybrid of the two would be worthwhile. Careful examination shows that the difference, in hardware, between the two resides in the fact that the Tracking type uses an up/down counter in place of the Successive Approximation Register. Since many presettable up/down counters are available, it appears possible to use the SAR output to load the counter and then switch to the Tracking configuration. This is the approach we are using. Our design allows this switchover to occur either automatically at the first End of Conversion signal from the Successive Approximation Register, or by programmed input from the CPU.

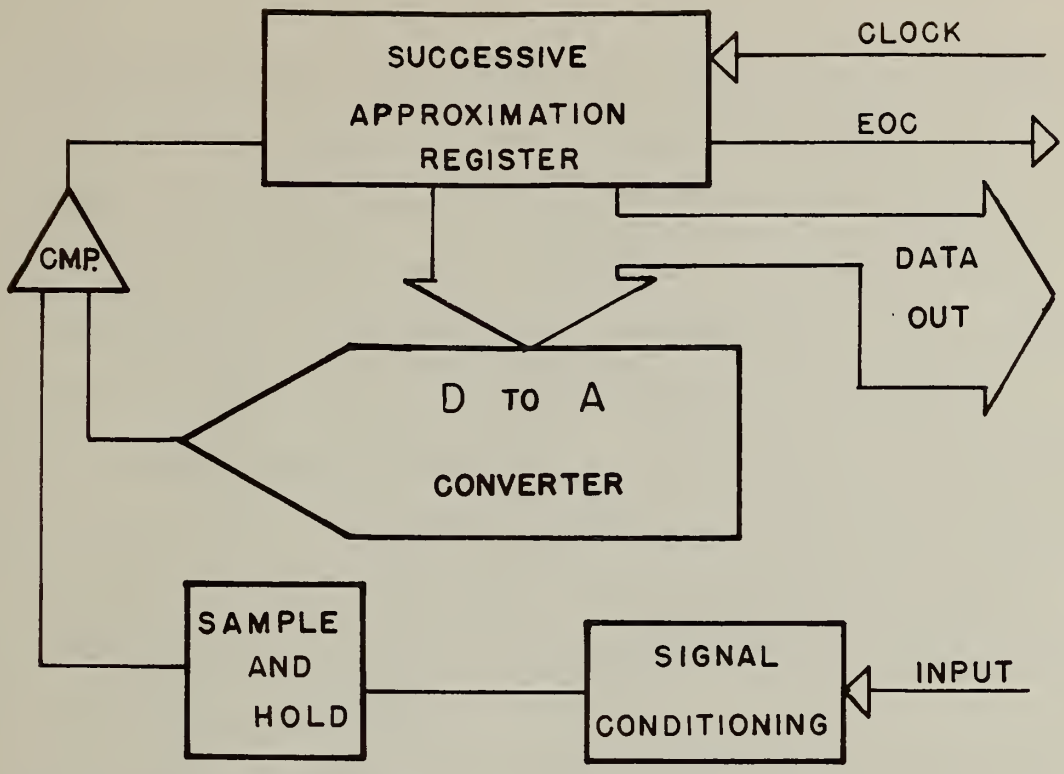

CMP. = COMPARATOR

Figure 30a. Block diagram of Successive Approximation ADC

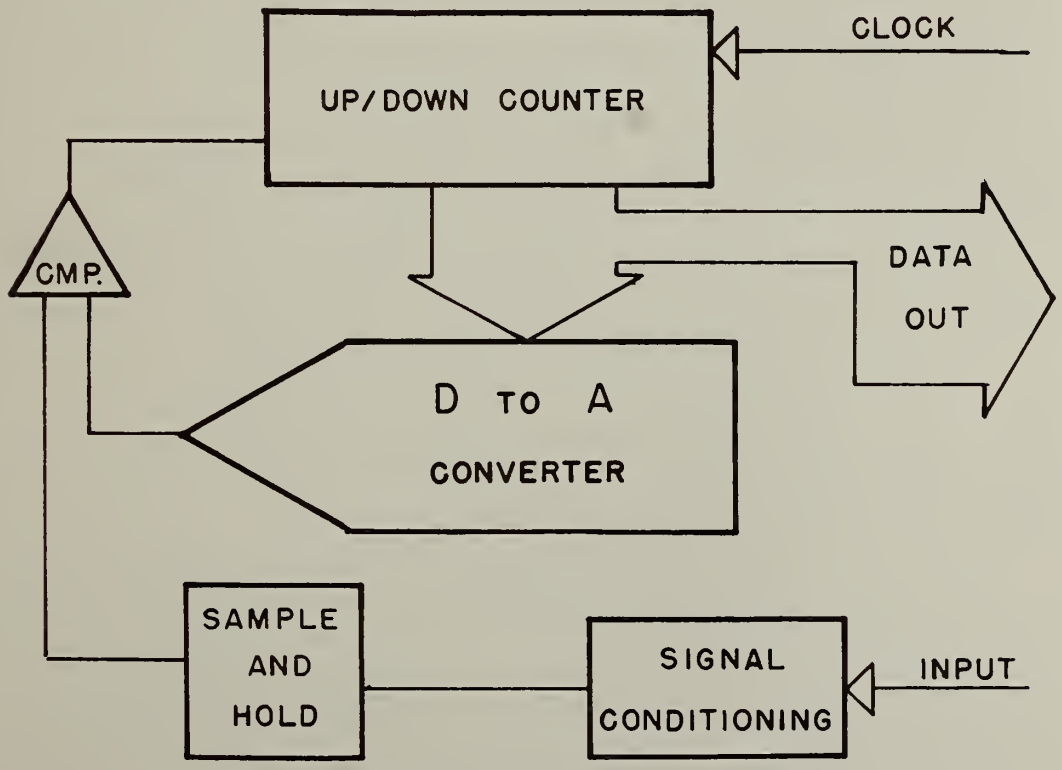

Figure 30b. Block diagram of Tracking Type ADC.

As discussed earlier, accesses to all converters are via registers that look like normal memory locations. However, the CPU actually loads data into the conversion board via a set of registers that are not accessible to a CPU read operation. Similarly, the μP cannot write into those registers that transfer data to the system bus. This procedure is followed in order to reduce the complexity of the required logic circuits. It also requires dedication of one DMA channel to data transfers to the converter board and another channel to transfers from the board.

Figures 31 through 35 are schematics of the resulting circuits after consideration of the above. A brief description of this board is given to highlight its features.

The DAC section contains 3 converters. DAC # 1 is a high speed (settling time less than 200 nsec.) 12 bit unit. Choice of either unipolar or bipolar operation is programmable, as is the gain of the output stage. Data can be input to the DAC by normal memory access or by DMA. The output is overvoltage protected and provision is made for low pass filtering if desired. The Sample and Hold is used for deglitching the output and has an acquisition time of less than 1 μs. Overall settling time for the entire system should be less than 4 μs, allowing operation (for output square waves) at frequencies up to 250 kHz.

DAC #2 and DAC #3 are slow speed 12 bit units. Operational control is similar to DAC #1 except that there is no DMA provided for. These converters operate at system settling times of about 12 μs. Thus, the maximum frequency out should be about 80 kHz (for square wave output). Provision is made for simultaneous or independent load and turn on of these devices. DAC #2 and DAC #3 are primarily intended for output to a plotter or to an external device (e.g. voltage controlled oscillator).

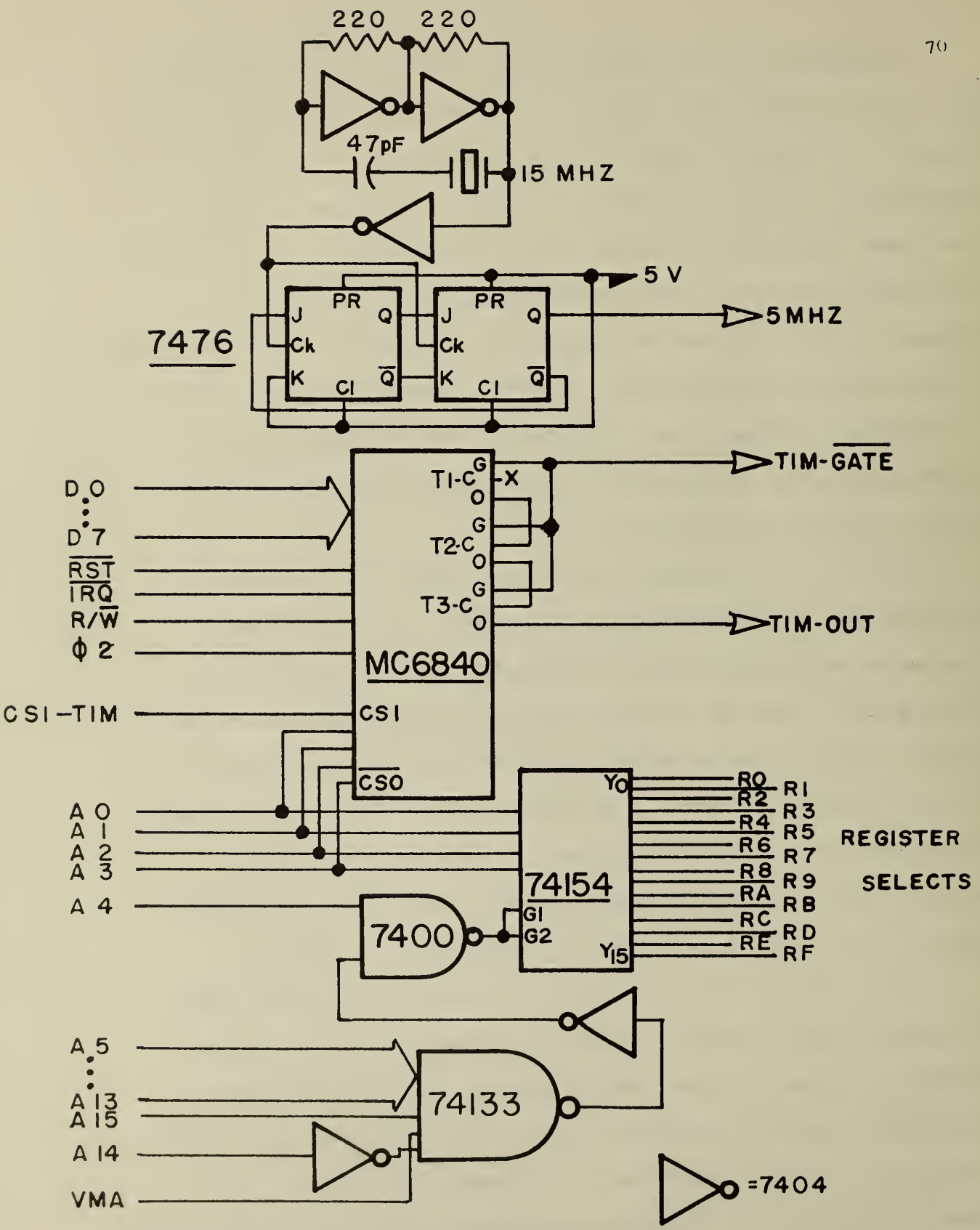

Figure 31. Schematic diagram of clock, timer and address decode section of converter board.

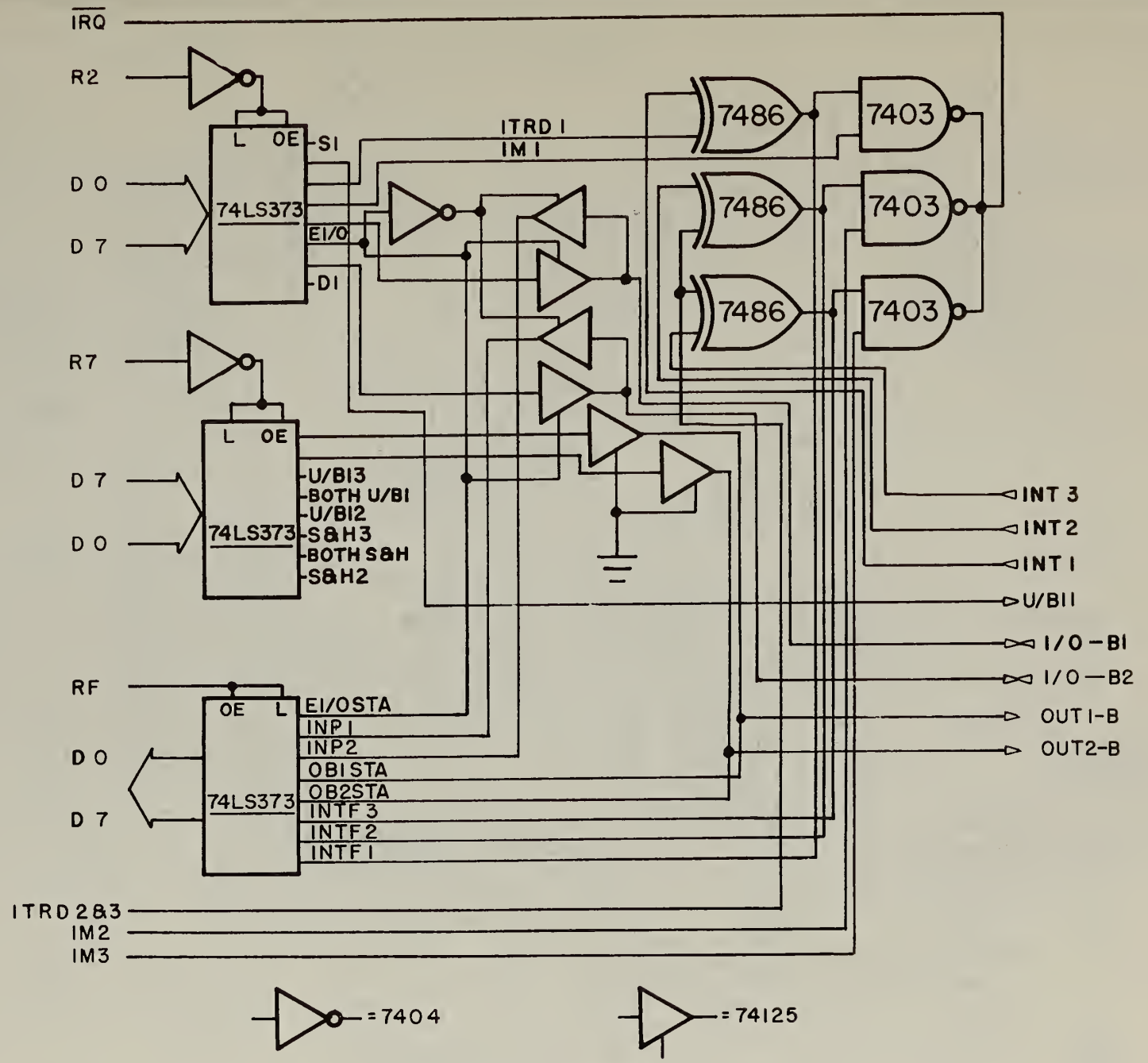

Figure 32. DAC control section schematic.

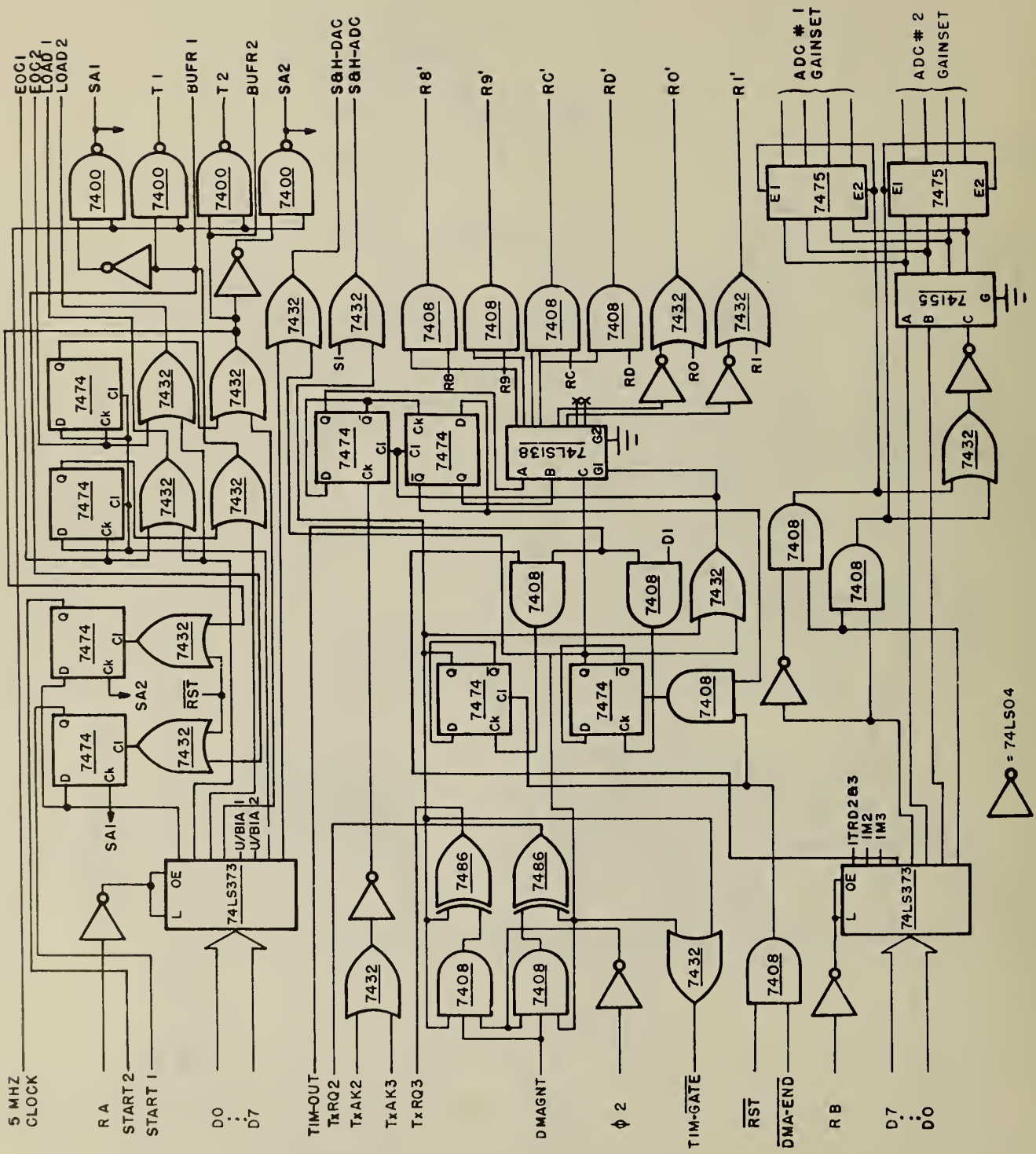

Figure 33. ADC control section schematic.

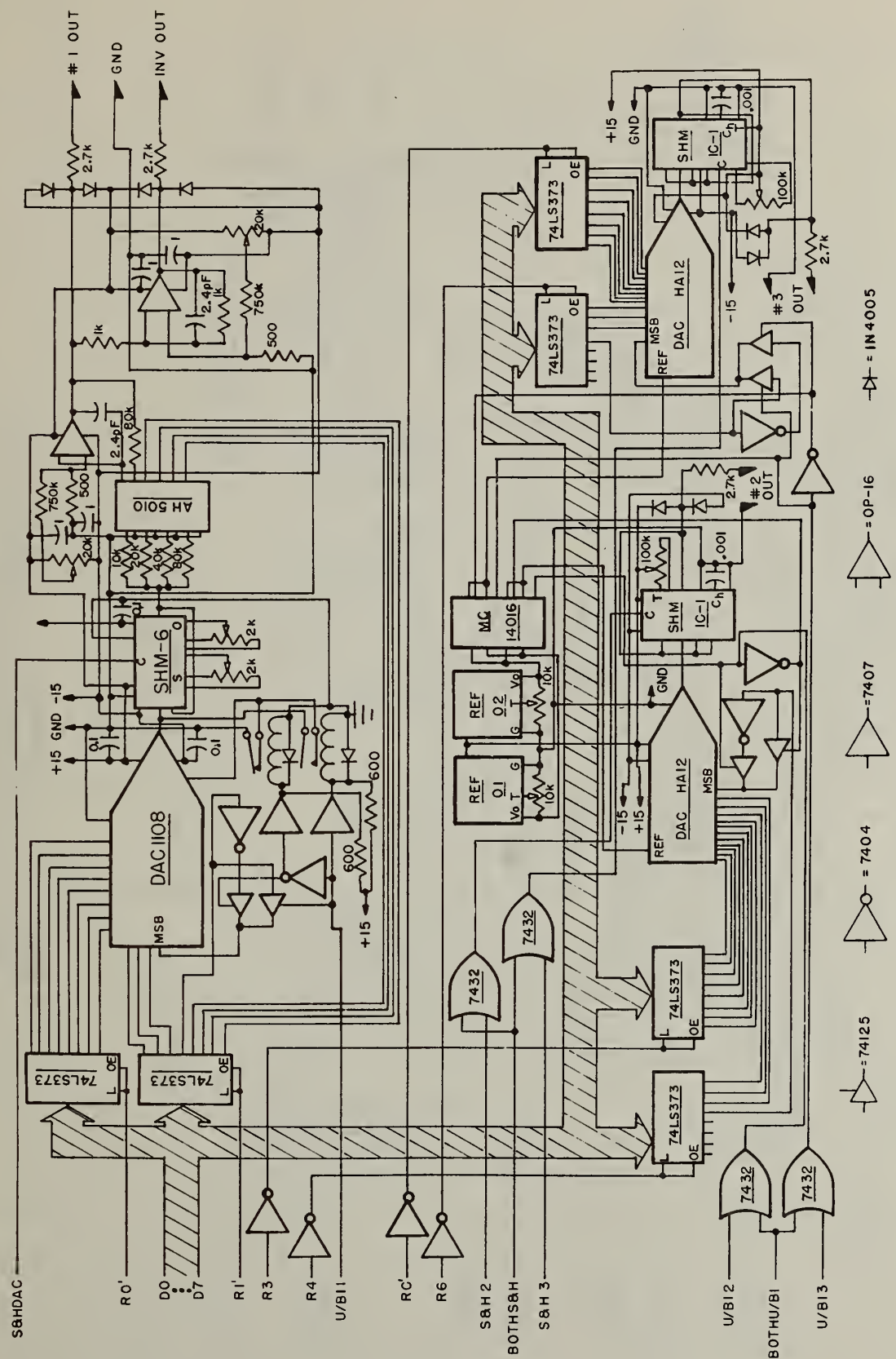

Figure 34. DAC converters.

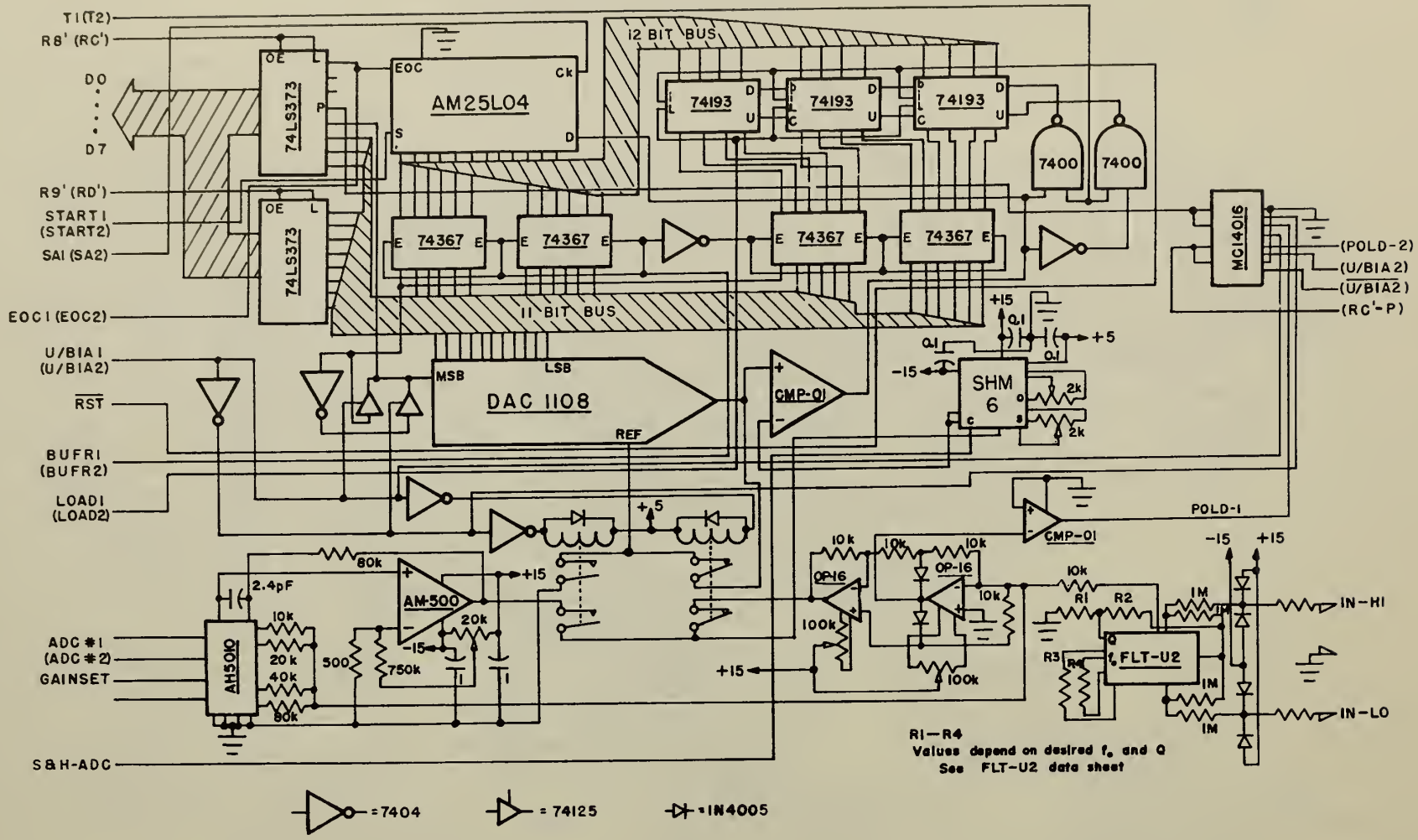

Figure 35. ADC converter #1 schematic. Converter #2 is identical with the necessary connections to the control section indicated by the number 2 in parenthesis.

ADC #1 and ADC #2 are identical units. They are high speed 12 bit devices. Each can be configured under program control as either a Successive Approximation or Tracking Type. They can be set to automatically switch from Successive Approximation to Tracking after initial signal acquisition, or to be switched at any desired time, if at all. Amplification of the overvoltage protected input signal is programmable as is choice of unipolar or bipolar operation. The input comes thru a low pass filter which attenuates signals of greater than 20 kHz by more than 80 dB. DMA operations or normal memory access is provided for. However, under DMA control both ADC's are read. There is no provision for a DMA read of only one converter (since all 4 DMA channels are being utilized).

This board provides for 2 logic level output lines and 2 selectable lines, the direction of which is under program control. Also provided are 3 maskable interrupt lines. Two of these have their transition directions controlled (as a pair) independently of the third.

2.3.3 Software

As indicated in section 2.3.2 some programming for the mass storage (Floppy disc) unit is being debugged. However, this is only the very minimum needed to drive the system for test purposes. (This will be adequate to read and write files to the disc but will not support all functions). A complete driver system is being written, and investigations into the possibility of obtaining a commercial Operating system are underway. (An Operating System [OS] is a program that coordinates all aspects of the software. It includes utility routines, file formating, etc. The peripheral routines - floppy disc drivers, converter board drivers, etc. - are assigned locations in the OS program, but must be written by the user). The ultimate driver program depends to some degree on the format of the OS but this is not limiting.

Drivers for the converter board have not been written since there is stlll some doubt as to the exact data form required (due to timing considerations which must be experimentally checked). Upon completion of the board* they will be written. This program should not be difficult due to the memory-mapping arrangement.

The primary programming effort has been devoted to Fast Fourier Transform (FFT) [45] programming. Speed considerations mandate that the program ultimately be written in assembly language. However, we at present have only an inadequate BASIC language program which will manage a 128 point FFT. It is based on a program from the literature [47] modified to suit our present purposes. An assembly language program for a 256 point (8 bit data) FFT has also been found in the literature [48]. This program requires extensive modification and revision before it can be used. Major modification to the addressing scheme used is needed before data of more than 8 bits can be used. Changes will also be needed to handle more than 256 points. However, it represents a useful starting point.

FFT programs for the present system are not expected to give us "real-time" outputs since at best they will take times measured in seconds. In order to obtain speeds unnoticeable to the operator, major hardware modifications would be needed. Such changes are not anticipated at this time.

---

*Completion is delayed due to delays in delivery of some parts.

References

1. R. L. Ripley, J. Less-Common Metals 4, 496 (1962).

2. L. H. Bennett, M. I. Cohen, A. L. Dragoo, A. D. Franklin, A. J. McAlister, and K. F. Young, Materials for Fuel Cells, NBSIR 78-1472, National Technical Information Service, Springfield, VA 22151.

3. L. H. Bennett, M. I. Cohen, A. L. Dragoo, A. D. Franklin, A. J. McAlister, and K. F. Young, Materials for Fuel Cells, NBSIR 77-1270, National Technical Information Service, Springfield, VA 22151.

4. W. Vogel, J. Lundquist, and A. Bradford, Electrochimica Acta 17, 1735, (1972); L. G. Austin and H. Lerner, Electrochimica Acta, 9, 1469 (1964).

5. R. S. Nicholson, Analytical Chem. 37, 1351 (1965).

6. D. W. Johnson, P. K. Gallagher, G. K. Wertheim, and E. M. Vogel, J. Catal. 48, 97 (1977).

7. J. O. Bockris and J. McHardy, J. Electrochem. Soc. 120, 61 (1973).

8. See S. Schicktanz, R. Kaiser, and W. Spengler, Solid State Com. 28, 935 (1978) and references therein.

9. W. Schottky, Wiss. Veroff. Siemenswerke, 14, H2, 1 (1935).

10. E. Baur and H. Preis, Z. Elektrochem., 43, 727 (1937).

11. K. Kiukkola and C. Wagner, J. Electrochem. Soc., 104, 379 (1957).

12. H. L. Tuller and A. S. Nowick, J. Electrochem. Soc., 122, 255 (1975).

13. T. Kudo and H. Obayashi, J. Electrochem. Soc., 122, 142 (1975); 123, 415 (1976).

14. J. W. Patterson, E. C. Bogren and R. A. Rapp, J. Electrochem. Soc., 114, 752 (1967).

15. A. S. Nowick and D. S. Park, "Fluorite-Type Oxygen Conductors," in Superionic Conductors, ed. by G. D. Mahan and W. L. Roth, Plenum Press (New York, 1976).

16. J. Lefevre, Ann. Chim., 8, 135 (1963).

17. R. Collongues, F. Quelyroux, M. Perez y Jorba and J. C. Gilles, Bull. Soc. Chim. Fr., 1141 (1965).

18. M. R. Thornber, D. J. M. Bevan and J. Graham, Acta Cryst., B24, 1183 (1968).

19. J. G. Allpress and H. J. Russell, J. Solid State Chem., 15, 68 (1975).

20. R. E. Carter and W. L. Roth, "Conductivity and Structure in Calcia-stabilized Zirconia," in Electromotive Force Measurements in High-Temperature Systems, ed. by C. B. Alcock, Elsevier (New York, 1968).

21. D. Michel, Mater. Res. Bull., 8, 943 (1973).

22. D. Michel, Rev. Int. Hautes Temp. Refract., 9, 225 (1972).

23. B. Hudson and P. T. Moseley, J. Solid State Chem., 19, 383 (1976).

24. W. H. Rhodes and R. E. Carter, J. Am. Chem. soc., 49, 244 (1966).

25. F. W. Lytle and H. H. Heady, Anal. Chem., 31, 809 (1959).

26. M. K. Carron, D. L. Skinner and R. E. Steven, Anal. Chem., 27, 1058 (1955).

27. K. S. Cole and R. H. Cole, J. Chem. Phys., 9, 341 (1941).

28. H. Juretschke, R. Landauer, and J. A. Swanson, Appl. Phys. 27, 838 (1956).

29. S. H. Chu and M. A. Seitz, J. Sol. State Chem. 23, 297 (1978)

30. J. Fouletier, P. Fabry, and M. Kleitz, J. Electrochem. Soc. 123, 204 (1976).

31. D. Y. Wang and A. S. Nowick, submitted to J. Electrochem. Soc. We thank Prof. Nowick for having allowed us to see this paper before publication.

32. M. I. Cohen and P. A. Heimann, NBS J. Research 83, 429 (1978).

33. IBM Diskette OEM Information GA 21-9190-1.

34. Motorola Corp. MC 6871A Microprocessor clock application Note R29-3-10. Revised (L-30-76).

35. W. C. Jung, IC Converter Cookbook, Howard W. Sams & Co., Inc. Indianapolis, Ind. p. 40, p. 49 (1978).

36. D. H. Sheingold, Ed. Analog-Digital Conversion Note Analog Devices, Inc., Norwood, Mass. p. 218 (1977).

37. E. R. Hnatek, Applications of Linear Integrated Circuits, John Wiley & Sons, New York, p. 59 (1975).

38. Ref. [35] p. 47 and Ref. [36] p. 224.

39. Ref. [35] p. 210.

40. L. R. Rabiner and R. W. Schafer, Digital Processing of Speech Signals, Prentice-Hall, Inc. Englewood Cliffs, NJ, p. 25 (1978).

41. Ibid. p. 26.

42. J. G. Graeme, Designing with Operational Amplifiers-Application Alternatives, McGraw-Hill Book Co., NY, p. 126 (1977).

43. J. Maxwell, Electronics, 50, No. 4, 99 (1977).

44. Ref. [35], p. 37.

45. Ibid p. 35.

46. E. O. Brigham, The Fast Fourier Transform, Prentice-Hall Inc., Englewood Cliffs, NY, p. 148 (1974).

47. W. Waggener, EDN, 23, No. 18, 80 (1978).

48. R. H. Lord, BYTE, 4, No. 2, 108 (1979).

NBS-114A (REV. 9-78)

U.S. DEPT. OF COMM. BIBLIOGRAPHIC DATA SHEET	1. PUBLICATION OR REPORT NO. NBSIR 80-1991	2. Gov't Accession No.	3. Recipient's Accession No.

4. TITLE AND SUBTITLE

MATERIALS FOR FUEL CELLS

5. Publication Date: MARCH 1980

6. Performing Organization Code

7. AUTHOR(S)
L. H. Bennett, C. K. Chiang, M. I. Cohen, A. L. Dragoo, A. D. Franklin, A. J. McAlister

8. Performing Organ. Report No.

9. PERFORMING ORGANIZATION NAME AND ADDRESS

NATIONAL BUREAU OF STANDARDS
DEPARTMENT OF COMMERCE
WASHINGTON, DC 20234

10. Project/Task/Work Unit No.

11. Contract/Grant No.

12. SPONSORING ORGANIZATION NAME AND COMPLETE ADDRESS *(Street, City, State, ZIP)*

13. Type of Report & Period Covered

14. Sponsoring Agency Code

15. SUPPLEMENTARY NOTES

☐ Document describes a computer program; SF-185, FIPS Software Summary, is attached.

16. ABSTRACT *(A 200-word or less factual summary of most significant information. If document includes a significant bibliography or literature survey, mention it here.)*

Transition metal-metalloid compounds involving V, Mo, Ta, and Nb with P, Si and N were examined as potential electrocatalyts in hot concentrated phosphoric acid. MoP, WP, $MoSi_2$, Mo_2N/MoN, and W_2N/WN were found to be stable in the absence of cathodic potentials. The W_2N/WN was non-conducting. $MoSi_2$ and Mo_2N/MoN were both inactive as catalysts and unstable under cathodic potentials. MoP and WP corroded at about 0.2 volts RHE. Only WP showed even mild activity as a hydrogen oxidation catalyst.

The electrochemical properties of $Mo_xW_{1-x}C$ electrodes were studied in some detail, and found to be independent of x near 0.7. The electrochemical behavior is very similar to that of WC, with about the same activity and the same indifference to CO poisoning.

Experiments are outlined for studying a possible "spillover" effect from Pt to $Mo_{1-x}W_xC$ and transition metal borides as supports, and for using a Raman spectroscopic technique for characterizing the electrochemical interface of transition metal-metalloid compound electrodes.

The preparation and characterization of high-density (99.6 to 99.8% of theoretical) Y_2O_3-doped CeO_2 ceramics is described. The material exhibits very sharp, single-phase, x-ray diffraction peaks, indicating good compositional homogeneity. The influence of various preparation methods on the sintering characteristics of powders of these materials is described. Chemical analytical techniques are given.

(Continued on attached sheet.)

17. KEY WORDS *(six to twelve entries; alphabetical order; capitalize only the first letter of the first key word unless a proper name; separated by semicolons)*

Catalyst; cerium dioxide; electrocatalysis; fuel cells; impedance; solid electrolyte; tungsten carbide.

18. AVAILABILITY ☒ Unlimited

☐ For Official Distribution. Do Not Release to NTIS

☐ Order From Sup. of Doc., U.S. Government Printing Office, Washington, DC 20402, SD Stock No. SN003-003-

☒ Order From National Technical Information Service (NTIS), Springfield, VA, 22161

19. SECURITY CLASS (THIS REPORT)	21. NO. OF PRINTED PAGES
UNCLASSIFIED	89
20. SECURITY CLASS (THIS PAGE)	**22. Price**
UNCLASSIFIED	$8.00

USCOMM-DC

ABSTRACT (continued)

The electrical properties of inhomogeneities, presumably grain-boundaries, in the Y_2O_3-doped CeO_2 ceramics were very different for materials prepared from powders produced by mixing the oxides from those found when the powders were prepared by coprecipitation. A higher resistance and a much higher capacitance were found in the latter case.

The temperature dependance of the inhomogeneity contribution to the overall resistance in the Y_2O_3-doped CeO_2 is somewhat different from that of the internal grain or crystal contribution, and since they are in series, the larger resistance dominates. At low temperatures it is the crystal contribution. Hence an Arrhenius plot of the dc conductivity exhibits a break, as often seen in the literature on these materials. Only the portion at temperatures above the break, on this view, represents the true properties of the substance itself.

In the course of 4-probe dc conductivity measurements on some Y_2O_3-doped CeO_2 materials a slow voltage transient was observed under constant-current conditions. This transient appears to involve a solid state diffusion process.

Modifications to our automated electrochemical measurement system are described that allow 1). an increase of the mass data storage available to the system, so that the results of a number of repetitive runs can be stored and later examined and compared; 2). an increase in the maximum sensitivity when data are being acquired at high speed, as in pulse mode operation; and 3). the use of a complete driver system in the software to coordinate all its aspects, and also the use of Fast Fourier Transform techniques during pulse mode operations. These modifications are described in detail.